Journal Pre-proof

Boundary Layer Tripping Effects on Flow and Trailing-Edge Noise of a NACA 0012 Airfoil at Zero Angle of Attack

Hussain A. Abid, Andrea Rapisarda, Vasily Gryazev,
Annabel P. Markesteijn, Nicola Maria Pugno, Sergey A. Karabasov

PII: S0022-460X(26)00439-6
DOI: https://doi.org/10.1016/j.jsv.2026.120078
Reference: YJSVI 120078

To appear in: *Journal of Sound and Vibration*

Received date: 25 March 2026
Revised date: 10 August 2026
Accepted date: 18 August 2026

Please cite this article as: Hussain A. Abid, Andrea Rapisarda, Vasily Gryazev, Annabel P. Markesteijn, Nicola Maria Pugno, Sergey A. Karabasov, Boundary Layer Tripping Effects on Flow and Trailing-Edge Noise of a NACA 0012 Airfoil at Zero Angle of Attack, *Journal of Sound and Vibration* (2025), doi: https://doi.org/10.1016/j.jsv.2026.120078

Highlights

Boundary Layer Tripping Effects on Flow and Trailing-Edge Noise of a NACA 0012 Airfoil at Zero Angle of Attack

Hussain A. Abid, Andrea Rapisarda, Vasily Gryazev, Annabel P. Markesteijn, Nicola Maria Pugno, Sergey A. Karabasov

- WMLES with Amiet and Brooks models are validated against BANC III experiments.
- Effects of trip height, width, and location on airfoil turbulence are quantified.
- Flow and turbulence are more sensitive to trip details at lower Reynolds numbers.
- Pressure fluctuations at the trailing edge are insensitive to trip parameters.

Boundary Layer Tripping Effects on Flow and Trailing-Edge Noise of a NACA 0012 Airfoil at Zero Angle of Attack

Hussain A. Abid[a,d], Andrea Rapisarda[b], Vasily Gryazev[c], Annabel P. Markesteijn[d], Nicola Maria Pugno[b,a], Sergey A. Karabasov[a,d,*]

[a]*School of Engineering and Materials Science, Queen Mary University of London, Mile End Road, London, E1 4NS, United Kingdom*
[b]*Mechano-X Labs, Department of Civil, Environmental and Mechanical Engineering, University of Trento, Via Mesiano, 77, Trento, 38123, Italy*
[c]*Department of Mechanical and Aerospace Engineering, Brunel University of London, Kingston Lane, Uxbridge, UB8 3PH, United Kingdom*
[d]*GPU-prime Ltd, Cambridge, United Kingdom*

Abstract

The study presents a series of Wall-Modelled Large Eddy Simulations (WMLES) using the high-resolution GPU-accelerated CABARET method to investigate boundary layer tripping effects on a NACA 0012 airfoil. Simulations are performed at zero angle of attack for chord-based Reynolds numbers of 1.0×10^6 and 1.5×10^6, corresponding to the BANC III experimental conditions. For far-field noise prediction, the LES solutions are coupled with Amiet theory and the semi-empirical Brooks model. The numerical framework is validated against experimental data for pressure and skin friction coefficients, boundary layer flow and turbulence profiles, as well as wall pressure and far-field noise spectra. Having validated the baseline model, the trip geometry is systematically varied to evaluate its effect on the flow, turbulence, and pressure fluctuations in the boundary layer and the wake region around the trailing edge using statistical analyses, including Proper Orthogonal Decomposition and conditional averaging. Compared to the meanflow and turbulence details, the pressure fluctuations around the trailing edge are found to be insensitive to the trip parameters within the experimental error bar, indicating that the dominant coherent pressure structures responsible for noise scattering remain little affected by the upstream transition-triggering mechanism.

Keywords: Trailing edge noise, Boundary layer tripping, Wall Modelled Large Eddy Simulation, Amiet method, GPU CABARET

*Corresponding author
Email address: `s.karabasov@qmul.ac.uk` (Sergey A. Karabasov)

1. Introduction

Broadband noise generated by turbulent boundary layers interacting with sharp trailing edges is a dominant component of airfoil self-noise in low-Mach number flows. As identified in the seminal work of Brooks, Pope, and Marcolini [1, 2], this trailing edge noise (TEN) constitutes the largest part of the broadband component and is produced by the scattering of multi-scale turbulent eddy pressure fluctuations at the sharp trailing edge. Recently, TEN has emerged not only as an important contributor to airframe noise but also as the dominant source of UAV rotor noise, where small propeller diameters and higher tip Mach numbers increase the relative importance of broadband noise compared to tonal noise [3]. TEN is notoriously difficult to accurately capture, even when computationally intensive scale-resolving methods such as Large Eddy Simulations are used. Hence, hybrid approaches, such as those based on acoustic analogy modelling, are traditionally used. The cornerstone of many TEN modelling approaches [4, 5] is the Amiet theory [6], which considers the problem of far-field noise generated by trailing edge scattering in terms of the wavenumber–frequency spectrum of wall surface pressure fluctuations induced by turbulent eddies. However, effective acoustic source information, namely the wavenumber–frequency spectrum, is typically only available from high-fidelity models such as Large Eddy Simulations (LES) [7, 8]. In a similar vein, the properties of the turbulent boundary layer are used in fast reduced-order TEN prediction schemes as input for correlations with far-field noise, such as in the original Brooks, Pope, and Marcolini (BPM) model [2]. Such TEN prediction schemes include several empirical calibration factors tailored for different experiments; these typically involve zero-camber airfoils like the NACA 0012, which serve as the "consensus" experimental data set for the validation of high-fidelity numerical models. Having a reference consensus data set is useful because of the inherent scatter between airfoil noise experiments in different wind-tunnel facilities. In particular, at Reynolds numbers typical of small-scale rotors and UAVs ($Re_c \sim 10^5$–10^6), the suction-side boundary layer may undergo laminar separation and reattachment, forming a laminar separation bubble (LSB). The LSB alters boundary layer thickness, turbulence development, and wall pressure spectra; it may also introduce tonal components through the growth of Tollmien–Schlichting (T–S) instability and trailing edge scattering. These phenomena are highly sensitive to the Reynolds number, upstream wind-tunnel conditions, and airfoil surface roughness [9, 10]. To avoid complexities of laminar flow separation and reattachment, tripping of the boundary layer is widely employed to enforce an earlier transition and suppress LSB dynamics, both in wind-tunnel experiments and in numerical simulations [11, 12]. Hence, tripping introduces the transition pathway leading to the development of turbulent structures in the boundary layer, directly influencing the wall pressure spectrum, the primary input to trailing edge noise models. Several experimental studies showed that trip height, geometry, and arrangement strongly influence transition onset and subsequent boundary layer development. For example, Abdalla et al. [13] and Chandrasekhara et al. [14] examined wire and strip trips on airfoils over $Re_c \approx O(10^5)$, demonstrating that insufficient trip height does not suppress laminar separation, while excessive roughness distorts velocity profiles and increases drag. Broadly, tripping devices can be classified into two-dimensional (2D) elements such as zigzag or straight strips and wires, and three-dimensional (3D) distributed roughness such as grit, cones, or sharkskin-like elements [15]. Following classical interpretations of roughness-induced transition [16], 2D trips promote transition through local separation and inflectional profiles that amplify T–S waves, while 3D roughness tends to generate turbulent spots directly downstream of the elements without relying on amplified T–S waves [17]. Dos Santos et al. [15] compared zigzag strips and grit over a range of h/δ_k and showed that zigzags produce localized regions of elevated turbulence intensity and spanwise non-uniformity, whereas grit yields a more uniform turbulent field once the flow is fully developed. Their measurements suggest that, provided the local momentum-thickness Reynolds number Re_θ is sufficiently high, the downstream TBL statistics become less sensitive to the detailed trip shape, although the near-trip dynamics can differ substantially. However, the focus of the above studies was primarily on aerodynamics such as viscous drag and the boundary layer thickness, while limited insight was provided on the tripping effect for the resulting wall surface pressure spectra and radiated noise. Recently, experimental aeroacoustic work has also begun to quantify the influence of different tripping concepts on far-field sound. Kang and Lee [18] reviewed common experimental tripping strategies at low Reynolds numbers relevant to UAVs, including trip wires, zigzag or serration strips, distributed grit, and bio-inspired sharkskin-type roughness. The tripping devices were found to induce transition through high-intensity spanwise velocity fluctuations. Additionally, the resulting low-frequency noise increases due to trip induced modifications of wall pressure fluctuations at trailing edge, whereas the trip itself can generate additional high-frequency noise. In their measurements, grid type roughness was less effective than zigzag strips at promoting transition below 20 m/s, leading to larger intermittency near the wake and discrepancies of up to 3 dB in far-field sound levels between the trip types [18]. These results suggest that the tripping parameters influence both the transition process and the resulting spectral distribution of the radiated noise. In high-fidelity computational modelling of TEN, an accurate representation of tripping is equally critical for reliable aeroacoustic prediction. LES investigations by Winkler et al. [4, 19] resolved thin serrated (zigzag) tape and a simplified two-dimensional step trip on a NACA 6512-63 airfoil at $Re_c = 1.9 \times 10^5$. The serration trip promoted early transition via oblique vortex patterns and T–S wave amplification, maintaining an attached turbulent boundary layer on the pressure side, whereas the step trip led to a separation bubble and later reattachment, with distinct differences in wall pressure evolution and noise levels. At higher Reynolds numbers, Morse and Mahesh [20] compared a geometrically resolved trip wire with a numerical tripping strategy based on steady wall-normal blowing on the DARPA SUBOFF hull. They showed that when the trip height exceeds the local laminar boundary layer thickness, the transition is dominated by shedding from the trip itself, altering turbulence anisotropy and leaving persistent differences in boundary layer thicknesses downstream even when skin friction and mean pressure recover. In addition to these efforts, Kang and Lee [18] contrasted geometrically resolved trips with artificial tripping techniques such as suction and blowing and high-frequency tangential reverse blowing, demonstrating that each mechanism produces scenario-specific acoustic signatures under adverse pressure gradients.

From the experimental perspective, recent work by Luesutthiviboon et al. [21] investigated the influence of trip height and location on a NACA 63_3-018 airfoil at several angles of attack, including the use of zigzag trips, in the framework of the Benchmark Problems for Airframe Noise Computations category I. That work reported data on integral aerodynamic coefficients as well as far-field sound pressure levels of the considered aerofoil cases and demonstrated that the trip modification can affect the far-field noise depending on the case. Collectively, the above-mentioned studies highlight that not only the presence of a trip, but also its geometry, placement, and underlying transition mechanism (T–S amplification, roughness-generated turbulent spots, or artificial forcing) can significantly influence both the near-wall pressure field and the far-field noise. Despite these advances, it remains difficult to separate the effect of geometric trip parameters from Reynolds-number effects, hence, to answer the question to what extent variations in trip geometry modify the near-wall turbulence responsible for trailing edge noise beyond simply triggering transition. Therefore, the aim of the present work is to perform high-fidelity scale-resolving simulations and analyse the results in terms of the wall-pressure fluctuations generated by the near-field turbulent structures to obtain a deeper physical interpretation of the flow mechanisms leading to the far-field acoustic response for a representative range of flow Reynolds numbers.

First, a wall-modelled large-eddy simulation (WMLES) is performed using the high-resolution CABARET method [22–24] for NACA0012 airfoil flow conditions at zero incidence angle, corresponding to the BANC-III benchmark dataset [25], where the step trip has been explicitly resolved. The WMLES solution is validated against the aerodynamic flow measurements available in the BANC-III test as well as the pressure and friction coefficients obtained from the semi-empirical X-Foil model. The wall-surface-pressure spectra solution from LES is combined with the Amiet formulation [6] including the back-scattering correction of Roger and Moreau [26] to obtain far-field noise spectra. In addition, the boundary layer quantities obtained from LES are used as input for the empirical BPM model [2] to independently probe the sensitivity of the LES solution for far-field noise spectra predictions. The resulting acoustic predictions obtained from the LES-Amiet and LES-BPM models are validated against the BANC-III experiment. Second, using the validated WMLES model, a parametric study is conducted to analyse the effects of trip height, trip width, trip location, and Reynolds number on transition behaviour, boundary layer development, and wall pressure spectra. Additionally, Proper Orthogonal Decomposition (POD) of turbulent fluctuating pressure field around the trailing edge is employed to identify dominant coherent structures and relate their evolution to the observed aeroacoustic trends.

2. Problem Configuration and Methods

2.1. Setup and Case Parameters

The BANC III cases are used for validation and assessment of the numerical framework, with flow conditions spanning $Re_c \sim \mathcal{O}(10^6–1.5\times10^6)$ as summarized in Table 1. Figure 1 shows a schematic of the computational problem setup, which corresponds to the conditions of the BANC III experimental campaign [25]. Specifically, a NACA 0012 airfoil at zero incidence with a chord length of $c = 0.4$ m is considered in a low Mach number free stream, representing a laboratory-scale test. Boundary layer tripping is applied to fix the transition point at a prescribed location on the airfoil surface, leading to the development of a turbulent boundary layer whose structures are subsequently scattered at the sharp trailing edge to generate far-field noise.

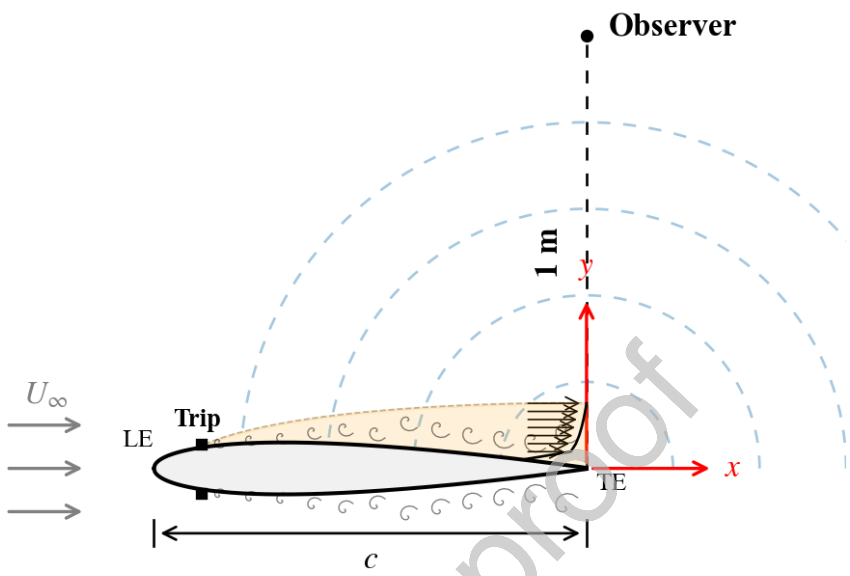

Figure 1: Schematic of the NACA 0012 airfoil, coordinate system, and observer location. The microphone is positioned 1 m vertically above the trailing edge (TE). Top and bottom trip devices are symmetrically positioned to preserve the axial symmetry of the NACA 0012 airfoil profile.

Table 1: Summary of BANC III [25] NACA 0012 test cases

Case	Angle of Attack (AoA)	Inflow Velocity U_∞ (m/s)	Reynolds Number Re_c	Mach Number M_∞
Case 1	0	56.0	1.5×10^6	0.166
Case 4	0	37.7	1.0×10^6	0.112

Following the BANC III experiment, a 2D stair-step trip is considered, characterized by its height h, tape width w, and streamwise position $x_t = x/c$ [25]. For each airfoil case, these parameters were systematically varied to analyze their effect on transition, boundary layer development, and far-field noise generation. The complete set of investigated configurations is summarized in Table 2, which also includes the dimensions used in the original experimental measurements and the empirical estimates for the effective trip height. In addition to the dimensional values, the trip height h and width w are reported in non-dimensional form using the maximum airfoil thickness as the reference length scale. For the present NACA 0012 airfoil with chord $c = 0.4$ m, the maximum thickness is $T_{\max} = 0.12c = 48$ mm; therefore, the ratios $h/T_{\max}$ and $w/T_{\max}$ quantify the relative size of the trip geometry with respect to the airfoil profile.

The trip heights h are selected to represent under-critical, near-critical, and over-critical roughness levels relative to the minimum effective height calculated via the empirical relation in Eq. (1). This effective trip height relation follows the roughness Reynolds number scaling suggested by Braslow and Knox [27]:

$$h = \frac{x_t}{\mathrm{Re}_{x_t}^{3/4}} \sqrt{\frac{\mathrm{Re}_h}{0.332}}, \tag{1}$$

where h is the trip height, Re_{x_t} is the Reynolds number evaluated at x_t, and Re_h is the roughness Reynolds number. This estimate provides a practical lower bound for triggering transition, typically associated with Re_h values in the range 200–600. Notably, the threshold depends on the trip geometry, with lower values generally sufficient for two-dimensional strip-type trips and higher values required for three-dimensional or distributed roughness elements [28, 29].

Table 2: Geometric parameters of the airfoil trips, with h and w non-dimensionalized by the maximum airfoil thickness, $T_{\max} = 48$ mm, and the trip position x_t reported as a percentage of the chord.

Numerical - 2D rectangular trip				
Height (h) (mm)	$h/T_{\max}$ (%)	**Width** (w) (mm)	$w/T_{\max}$ (%)	**Position** (x_t) %c
0.127	0.26	1.50	3.13	5
0.360	0.75			
0.554	1.15			
1.018	2.12			
0.360	0.75	0.53	1.10	5
		1.50	3.13	
		2.31	4.81	
		4.24	8.83	
0.360	0.75	1.50	3.13	5
				10
				20
				25
				30

Experimental [25] - 2D rectangular trip				
Height (h) (mm)	$h/T_{\max}$ (%)	**Width** (w) (mm)	$w/T_{\max}$ (%)	**Position** (x_t) %c
0.360	0.75	1.50	3.13	5

Empirical relation based on roughness Re number (1)				
Height (h) (mm)	$h/T_{\max}$ (%)	**Width** (w) (mm)	$w/T_{\max}$ (%)	**Position** (x_t) %c
0.250	0.52	-	-	5

2.2. Large Eddy Simulation Method and Grids

For high fidelity modelling of the BANC-III airfoil cases considered, a WMLES framework based on the high-resolution Compact Accurately Boundary-Adjusting High-Resolution Technique (CABARET) scheme [22, 30], accelerated on Graphics Processing Units (GPUs) [31] is used. CABARET combines a finite-volume formation in space-time with conservative flux correction based on the maximum principle, and low-dissipation and low-dispersion wave propagation properties important for accurate reconstruction of statical properties of advection-dominated stochastic flows and turbulent jets [32, 33]. The asynchronous algorithm is used to efficiently time step with a Courant number corresponding to the optimized dispersion and dissipation properties for acoustic wave propagation [23, 34]. Viscous terms are approximated by a central scheme, where the wall shear stress is approximated with the equilibrium wall model of Park [35]. The model adopts an algebraic formulation based on Reichardt's law [36], relating the local dimensionless velocity u^+ and wall-normal distance y^+. Previous validation of the CABARET-based WMLES framework for NACA airfoils, including a NACA 0012 airfoil with chord length $c = 0.4$ m and a NACA 65410 airfoil with chord length $c = 0.3$ m, over a range of inflow Reynolds numbers and angles of attack, can be found in [37, 38].

The current work presents a systematic investigation of the CABARET WMLES of the NACA 0012 airfoil with a chord length of 0.4 m, where the laminar-to-turbulent transition is explicitly controlled using a leading-edge step trip, whose parameters h, w, and $x_t = x/c$ are varied to analyse the effect on transition and acoustic response. The computational domain extends $10c$ upstream and $10c$ downstream of the airfoil, with a wall-normal extent of $\pm 10c$. The spanwise length is set to $L_z/c = 0.10$ for all configurations. The domain is discretised using a hexahedral dominant mesh with multiple local refinement zones generated in OpenFOAM. Near the airfoil surface, body-fitted hexahedral layers are created using `snappyHexMesh` to control the first-cell height and wall spacing, with additional refinement in the leading-edge region to resolve the trip geometry (Fig. 2). The step trip is resolved with 4 cells across a representative trip height of $h = 0.360$ mm ($0.75\%\, T_{\max}$) and 12 points across a representative trip width of $w = 1.50$ mm ($3.13\%\, T_{max}$). Notably, due to the CABARET staggered cell-centre and cell-face variables, these 4 and 12 grid cells correspond to 9 and 25 data points, respectively.

For all configurations under investigation, non-reflecting characteristic boundary conditions are applied for all external boundaries with a uniform inflow velocity prescribed at the inlet and the free-stream conditions at the top, bottom, and downstream boundaries. Periodic boundary conditions are imposed in the spanwise direction. The computational mesh for all setups contains approximately 39.1 million cells, with near-wall grid spacings in wall units of $\Delta x_1^+ = 16$ (streamwise), $\Delta x_2^+ = 3$ (wall-normal), and $\Delta x_3^+ = 17$ (spanwise). The wall-normal grid is refined with an expansion ratio of 1.2, ensuring that three grid cells (7 data cell and face points) are located within the near-wall region up to $x_2^+ = 19$. These grid resolution parameters were found sufficient to produce the main flow and

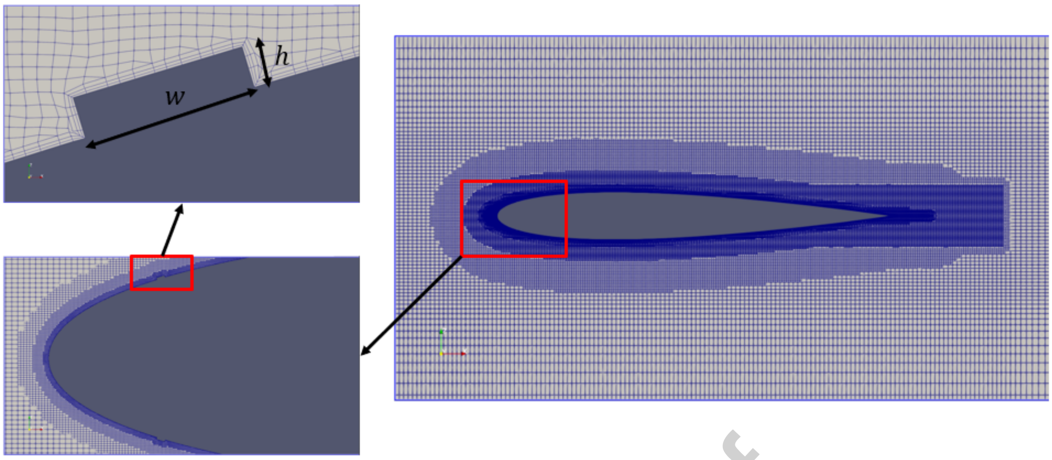

Figure 2: Computational mesh topology for the NACA 0012 airfoil showing the leading-edge step trip (top left), the leading-edge region (bottom left), and the overall mesh distribution around the airfoil (right).

turbulence profiles, including the C_p, C_f, and wall pressure spectra reasonably insensitive to further grid refinements.

All simulations were performed on an NVIDIA A100 GPU (80 GB) using the Apocrita High-Performance Computing Cluster at Queen Mary University of London. Each case was run for five convective time units (TU) to allow for flow development, followed by an additional 25 TU for statistical averaging, where TU $= c/U_\infty$. To efficiently time step in the mesh regions corresponding to different local refinements, eight update groups of the asynchronous time-stepping scheme were used, resulting in a time-step ratio of $2^7 = 128$ between the time steps used for the smallest and the largest grid cell sizes.

2.3. *Far-Field Acoustic Modelling*

The influence of the trip parameter on the farfield noise is evaluated using two approaches: the analytical Amiet trailing edge noise model [6] and the empirical BPM method [2] using the input flow parameters from the LES data for each test case.

2.3.1. *Amiet Trailing edge noise model*

Amiet trailing edge noise model provides a theoretical framework for predicting broadband noise generated by the interaction of a turbulent boundary layer with a sharp trailing edge. The model relates the surface pressure fluctuations convecting within the boundary layer to the farfield acoustic pressure through a wavenumber–frequency formulation under the frozen turbulence assumption. The Amiet approach has been extensively used for the prediction of trailing edge noise for both symmetric and cambered NACA airfoils using experimental wall-surface measurements and scale-resolving computational modelling [19, 37, 39] where both zigzag and step-type tripping configurations were applied to force transition. In the present study, the far field power spectral density, $S_{\mathrm{pp}}(\omega)$, is computed using the Amiet trailing edge noise model, where the source terms, surface pressure spectrum, spanwise correlation length scale $\Lambda_{\mathrm{pp}|3}$, and convection velocity U_{c} are obtained directly from the LES data. The model accounts for both the high frequency noise, where the airfoil acoustically behaves as a semi-infinite flat plate and the lower frequencies, where finite-chord effects are incorporated through the back-scattering correction of Roger and Moreau [26] valid for realistic airfoil geometries in low Mach number flow conditions [39]. The noise power spectral density of the Amiet model and the corresponding correlation length scale $\Lambda_{\mathrm{pp}|3}$ and convection velocity U_{c} parameters are given as Eqs. (2) and (3):

$$S_{\mathrm{pp}}\left(x_1, x_2, x_3 = 0; \omega\right) = \left(\frac{\omega c x_2}{4\pi c_0 \sigma^2}\right)^2 \frac{L_3}{2} \left|\mathscr{L}\left(\frac{\omega}{U_{\mathrm{c}}}, k_3 = 0, x_1, x_3\right)\right|^2 \Lambda_{\mathrm{pp}|3} \Pi_{\mathrm{w}}\left(\omega\right) \tag{2}$$

$$\Lambda_{\mathrm{pp}|3}(\omega) = 1.4\frac{U_{\mathrm{c}}}{\omega}, \quad U_{\mathrm{c}} = 0.70 U_\infty. \tag{3}$$

Here, $S_{\rm pp}(x_1, x_2, x_3 = 0; \omega)$ is the power spectral density (PSD) of the acoustic pressure at an observer located at angular frequency ω. The coordinate origin is located at the trailing edge, where $x_1 = 0$ corresponds to the edge and $x_3 = 0$ to mid-span. The acoustic transfer function $\mathscr{L}$ is given by:

$$\left|\mathscr{L}\left(\frac{\omega}{U_{\rm c}}, k_3 = 0, x_1, x_3\right)\right| = \frac{\mathrm{e}^{2\mathrm{i}A}}{\mathrm{i}A}\left\{(1+\mathrm{i})\mathrm{e}^{-2\mathrm{i}A}\sqrt{2B}\,E_{\rm s}^*[2(B-A)] - (1+\mathrm{i})\,E^*[2B]\right\}, \tag{4}$$

with the associated complex functions and phase terms defined as:

$$E_{\rm s}(z) = \frac{E^*(z)}{\sqrt{z}}, \quad E^*(z) = \frac{1-\mathrm{i}}{2}\,\mathrm{erf}\left(\sqrt{\mathrm{i}z}\right), \tag{5}$$

and

$$A = \frac{\omega}{U_{\rm c}}\,b + \frac{\omega b}{c_0\beta_{\rm c}^2}\left(M_\infty - \frac{x_1}{\sigma}\right), \quad B = \frac{\omega}{U_{\rm c}}\,b + \frac{\omega b}{c_0\beta_{\rm c}^2}\left(M_\infty + 1\right). \tag{6}$$

In the above formulations, $\mathscr{L}$ represents the trailing edge acoustic scattering transfer function. The geometric and flow parameters include the airfoil chord c, semi-chord b, span L_c, and speed of sound c_0. $U_{\rm c}$ is the convection velocity of turbulent eddies and M_∞ is the free-stream Mach number. The term $\sigma^2 = x_1^2 + \beta_{\rm c}^2(x_2^2 + x_3^2)$ accounts for the flow-corrected radiation distance, where $\beta_{\rm c} = \sqrt{1 - M_\infty^2}$ is the compressibility correction. Additional source terms include the spanwise wavenumber k_3, the spanwise correlation length of surface pressure fluctuations $\Lambda_{\rm pp|3}$, and the trailing-edge surface pressure spectrum $\Pi_{\rm w}(\omega)$. The functions $E^*(z)$ and $E_{\rm s}(z)$ are complex Fresnel-type integrals, with $\mathrm{erf}(\cdot)$ denoting the complex error function.

2.3.2. BPM Model

The BPM model is an empirical framework for predicting general self-noise, including turbulent boundary layer trailing edge noise, separated flow noise, and vortex shedding noise, derived from extensive wind-tunnel measurements of symmetric airfoils [2]. Each noise component of BPM is represented through empirical correlations calibrated against experiments, requiring only basic boundary layer parameters as input. The BPM model for the one-third-octave-band sound pressure level at a given frequency f is:

$$\mathrm{SPL}_{\rm BPM}(f) = F(\delta^*, U_\infty, c, \theta, \alpha, \mathrm{Re}_c, \ldots) \tag{7}$$

Functional parameters of the BPM model include boundary layer displacement thickness δ^*, free-stream velocity U_∞, chord length c, observer angle θ, angle of attack α, Reynolds number based on chord Re_c, and observer distance $r = \sqrt{x_1^2 + x_2^2 + x_3^2}$, where (x_1, x_2, x_3) are the observer coordinates relative to the trailing edge. The frequency dependence f and empirical corrections for Mach number and directivity are also included in the model, the expression for trailing edge noise spectra being:

$$\mathrm{SPL}_{\rm TBL--TE}(f) = K_1 + 10\log_{10}\left(\frac{\delta^* M_\infty^5 L D_{\rm h}}{r_{\rm e}^2}\right) + K_2(\alpha, \mathrm{Re}_c) + D(\theta, M_\infty) + G(f, \delta^*, U_\infty), \tag{8}$$

where K_1 is an empirical constant, K_2 provides angle of attack and Reynolds number corrections, D is the directivity term, and G is an empirical spectral shape function. The spectral-shape function is given as:

$$G(f, \delta^*, U_\infty) = 10\log_{10}\left(\frac{\mathrm{St}^2}{\left(1 + \mathrm{St}^2\right)^{7/3}}\right), \tag{9}$$

where St is the Strouhal number, defined as:

$$\mathrm{St} = \frac{f\delta^*}{U_\infty}. \tag{10}$$

In the original publication of the BPM model, boundary layer development over the NACA 0012 airfoil was examined for both clean (untripped) and tripped conditions. In the clean case, the smooth surface allowed a naturally developing laminar boundary layer. In the tripped case, transition was forced using randomly distributed grit strips from the leading edge to approximately 20% of the chord, generating a fully turbulent boundary layer while maintaining geometric similarity across different airfoil sizes.

In addition, empirical correlations were introduced using hot-wire measurements near the trailing edge. These helped determining the turbulent boundary layer thicknesses on the suction side, δ_s, as a function of the chord-based Reynolds number Re_c and angle of attack α. Compared to the pressure side, the suction side of the airfoil is typically responsible for most of the trailing edge noise; hence, only the suction side parameters will be considered here. In particular, the corresponding approximation for the boundary layer thicknesses on the suction side, normalized by chord length, is given in Eq. (11):

$$\delta_\mathrm{s} = \begin{cases} 10^{0.0311\alpha} \cdot \mathrm{BL}_0 & 0 \le \alpha \le 5^\circ \\ 0.3468 \cdot 10^{0.1231\alpha} \cdot \mathrm{BL}_0 & 5^\circ < \alpha \le 12.5^\circ \\ 5.718 \cdot 10^{0.0258\alpha} \cdot \mathrm{BL}_0 & 12.5^\circ < \alpha \le 25^\circ \end{cases} \tag{11}$$

where BL_0 denotes the boundary layer thickness at zero angle of attack:

$$\mathrm{BL}_0 = 10^{1.892 - 0.9045\log_{10}(\mathrm{Re}_c) + 0.0596(\log_{10}(\mathrm{Re}_c))^2} \cdot c. \tag{12}$$

Displacement thicknesses at the trailing edge also follow similar relations. The zero-degree angle of attack displacement thickness δ_0^* is given by:

$$\delta_0^* = \begin{cases} 0.0601 \cdot \mathrm{Re}_c^{-0.114} \cdot c & \mathrm{Re}_c \le 3 \times 10^5 \\ 10^{3.411 - 1.5397\log_{10}(\mathrm{Re}_c) + 0.1059(\log_{10}(\mathrm{Re}_c))^2} \cdot c & \mathrm{Re}_c > 3 \times 10^5, \end{cases} \tag{13}$$

which expression is used to calculate the suction-side displacement thickness:

$$\delta_\mathrm{s}^* = \begin{cases} 10^{0.0679\alpha} \cdot \delta_0^* & 0 \le \alpha \le 5^\circ \\ 0.381 \cdot 10^{0.1516\alpha} \cdot \delta_0^* & 5^\circ < \alpha \le 12.5^\circ \\ 14.296 \cdot 10^{0.0258\alpha} \cdot \delta_0^* & 12.5^\circ < \alpha \le 25^\circ \end{cases} \tag{14}$$

Together with the boundary layer thickness parameter δ_s, the displacement thickness δ_s^* is used as input in the empirical formula (see Eq. (8)) to compute the trailing edge noise spectrum.

2.4. Proper Orthogonal Decomposition of near-field pressure fluctuations

To analyse the effect of the trip on the turbulent pressure fluctuations around the airfoil trailing edge, Proper Orthogonal Decomposition (POD) was applied following the work of Lumley [40]. Because the available LES time signal is limited, the snapshot POD method of Sirovich [41] was used. To improve the statistics available to the POD, the pressure field was extracted on 10 spanwise planes stacked across the airfoil span, $z/L_c \in [-0.018, +0.018]$, in the vicinity of the trailing edge, as shown in Fig. 3.

At each time instant t, assuming the airfoil span direction is statistically homogeneous, the pressure fields are averaged across the available planes to form a single plane-averaged dataset $p_\mathrm{avg}(\boldsymbol{x}, t)$. This spatial averaging effectively selects the dominant symmetric pressure mode, thereby reducing the dimensionality of the problem to simplify the POD analysis. The temporal average of this symmetric pressure mode is computed as:

$$\bar{p}_\mathrm{avg}(\boldsymbol{x}) = \frac{1}{T}\int_0^T p_\mathrm{avg}(\boldsymbol{x}, t)\,\mathrm{d}t, \tag{15}$$

where T denotes the total sampling duration. This mean field is then used to calculate the fluctuation field:

$$Q(\boldsymbol{x}, t) = p_\mathrm{avg}(\boldsymbol{x}, t) - \bar{p}_\mathrm{avg}(\boldsymbol{x}). \tag{16}$$

The resulting pressure fluctuations are arranged into the snapshot matrix:

$$\mathbf{Q} = \left[Q(\boldsymbol{x}, t_1), Q(\boldsymbol{x}, t_2), \ldots, Q(\boldsymbol{x}, t_{N_\mathrm{t}})\right], \tag{17}$$

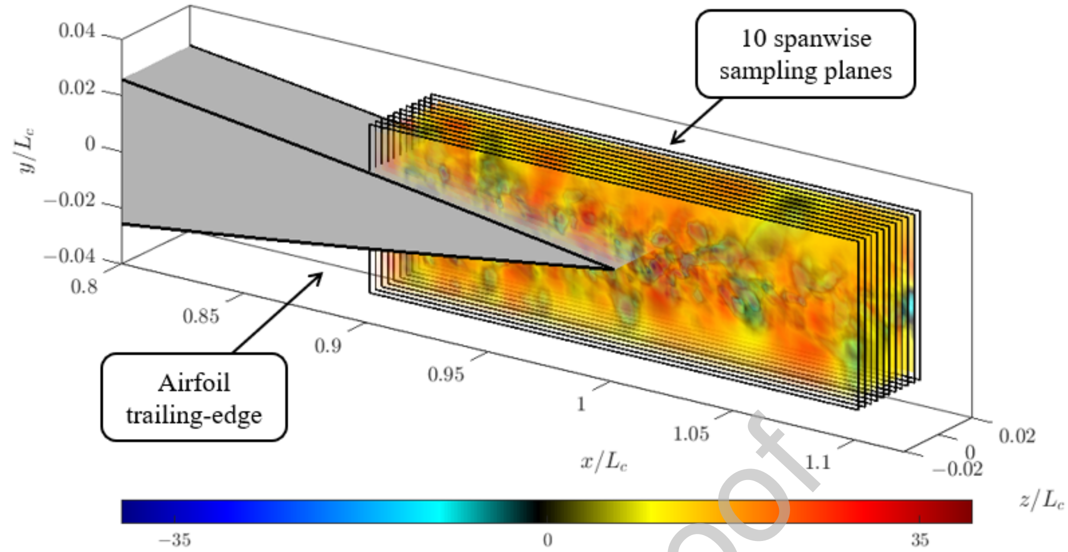

Figure 3: Instantaneous near-field pressure fluctuation, $Q(\mathbf{x}, t)$ (Eq. (16)), sampled on the ten spanwise planes used for the POD analysis.

where N_t is the total number of snapshots. To obtain the eigenmodes, the singular value decomposition (SVD) is performed:

$$\mathbf{Q} = \mathbf{U}\mathbf{\Sigma}\mathbf{V}^{\mathrm{T}}, \tag{18}$$

where $\mathbf{U}$ contains the spatial orthonormal modes, $\mathbf{\Sigma}$ is a diagonal matrix of singular values σ_j, and $\mathbf{V}$ contains the corresponding temporal orthonormal modes. The spatial POD modes are therefore given by:

$$\phi_j(\boldsymbol{x}) = \mathbf{u}_j(\boldsymbol{x}), \tag{19}$$

where $\mathbf{u}_j$ denotes the j-th column of $\mathbf{U}$. The associated energy per POD mode is given by:

$$\lambda_j = \sigma_j^2, \tag{20}$$

where λ_j is the eigenvalue of the j-th POD mode. To characterize the spectral distribution of the turbulent fluctuations, the relative energy contribution E_j of each mode is expressed as a percentage:

$$E_j(\%) = 100 \times \frac{\lambda_j}{\sum_{i=1}^{N_t} \lambda_i}, \tag{21}$$

where N_t is the total number of modes. The corresponding temporal coefficients are obtained as:

$$a_j(t_k) = \sigma_j V_j(t_k), \tag{22}$$

where $a_j(t)$ denotes the amplitude of mode j. Following the POD method, the pressure fluctuation field can be approximated by the truncated expansion:

$$Q(\boldsymbol{x}, t) = \sum_{j=1}^{m} \phi_j(\boldsymbol{x}) a_j(t), \tag{23}$$

where m denotes the number of retained modes.

2.5. *Workflow process based on the LES, Amiet, BPM, and POD models*

The integrated numerical framework for far-field noise prediction is illustrated in Fig. 4. The WMLES database is post-processed using two prediction models. For the analytical model based on Amiet's trailing-edge noise theory, the wall-pressure spectrum $\Pi_w(\omega)$, spanwise pressure-correlation length $\Lambda_{pp|3}(\omega)$, and convection velocity U_c are extracted near the trailing edge. For the semi-empirical BPM model, the boundary-layer thickness δ and displacement thickness δ^* are extracted from the same WMLES solution and used as model inputs.

The two models provide independent far-field acoustic estimates. Amiet's theory gives the far-field pressure spectral density $S_{pp}(f)$, which is converted into one-third-octave sound pressure levels for comparison with measurements, whereas the BPM model directly provides the turbulent-boundary-layer trailing-edge noise spectrum, $\mathrm{SPL}_{\mathrm{TBL-TE}}(f)$. The parallel use of analytical and semi-empirical formulations provides a consistent basis for assessing the LES-derived flow statistics against the experimental acoustic data.

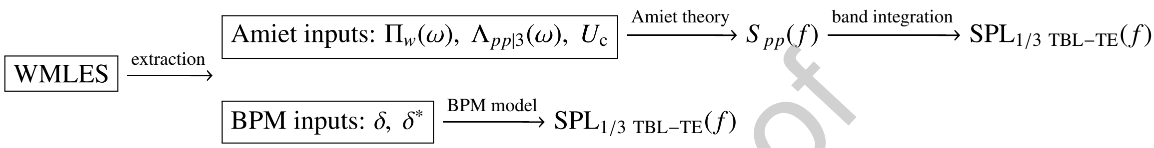

Figure 4: Workflow for far-field noise prediction. Flow statistics extracted from the WMLES are used as inputs to Amiet's analytical trailing-edge noise theory and the empirical BPM model.

Having performed the validation of the flow and acoustic solutions against the BANC III experimental data [25], the framework is then extended to a systematic parametric study. As summarized in Fig. 5, this study quantifies the sensitivity of the trailing edge flow physics, specifically turbulence intensity and pressure fluctuations, to variations in trip height, width, and location.

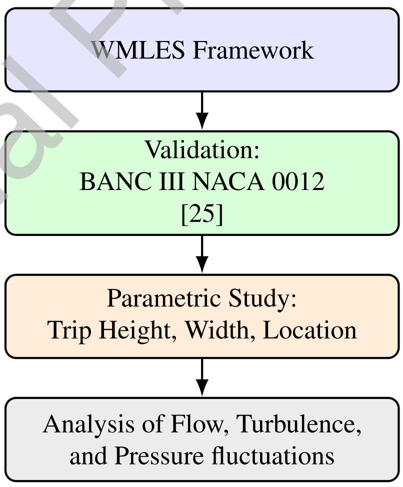

Figure 5: Workflow of the computational modelling for the BANC III test case

3. Results and Discussion

3.1. *Validation*

Following the BANC-III experiment, the NACA 0012 airfoil at zero incidence is considered at two chord-based Reynolds numbers, $\mathrm{Re}_c = 1.5 \times 10^6$ and $\mathrm{Re}_c = 1.0 \times 10^6$. These correspond to free-stream velocities of $U_\infty = 56$ m/s and $U_\infty = 37.7$ m/s, respectively. A stair-step trip is located at $x_\mathrm{t}/c = 0.05$, with a height of $h = 0.360$ mm and a width of $w = 1.50$ mm (see Tables 1 and 2). In what follows, the flow solutions obtained in terms of the airfoil wall surface and boundary layer quantities as well as the far-field noise spectra are compared with the experimental results.

3.1.1. *Pressure and friction coefficients*

Fig. 6 compares the distributions of the pressure coefficient C_p and skin friction coefficient C_f with experimental data. Comparisons with predictions of the empirical XFOIL model are shown on the same plots. The computed C_p distributions from LES show excellent agreement across the chord for both wind velocities. Notably, not only is the overall shape of the pressure coefficient accurately captured in the LES solution, but the suction peak due to the trip is also in excellent agreement with the experiment.

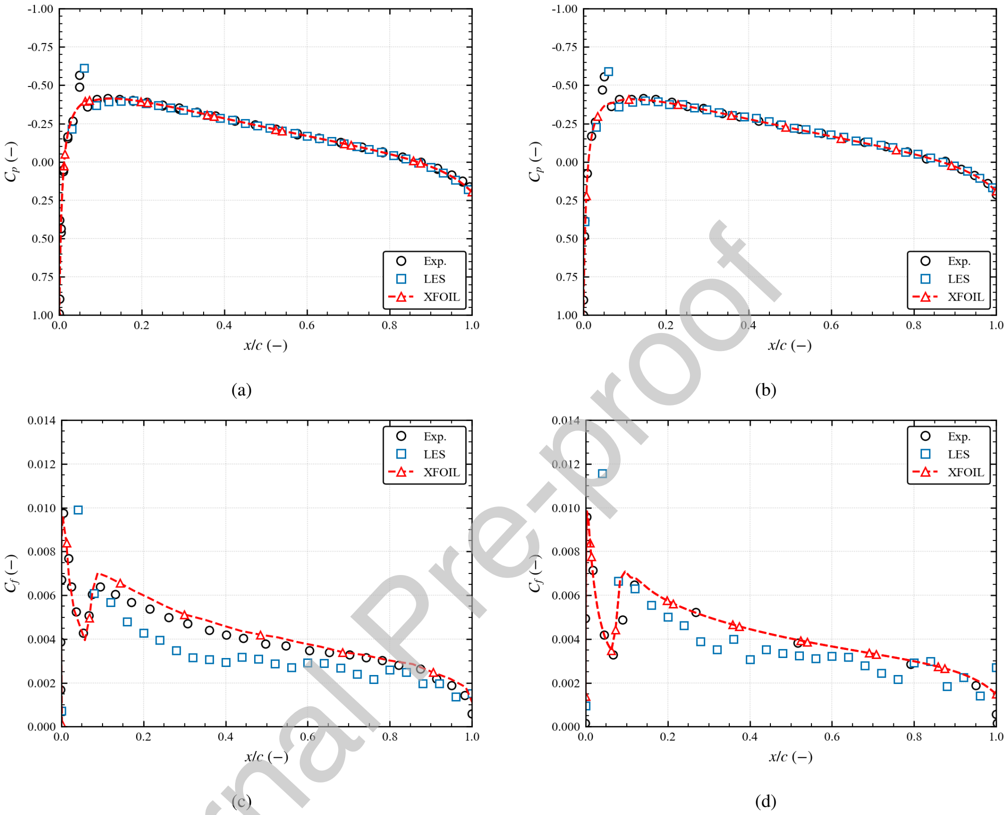

Figure 6: Comparison of the pressure coefficient C_p for (a) $\mathrm{Re}_c = 1.5 \times 10^6$ and (b) $\mathrm{Re}_c = 1.0 \times 10^6$, and the skin-friction coefficient C_f for (c) $\mathrm{Re}_c = 1.5 \times 10^6$ and (d) $\mathrm{Re}_c = 1.0 \times 10^6$, comparing the WMLES results (LES), BANC-III experiment (Exp.), and empirical XFOIL model.

The predicted C_f distributions of the LES reproduce the general trends in the development of the boundary layer, including the rapid variation in the region near the leading edge, including the area of the trip, and gradual decay toward the trailing edge. At $U_\infty = 56$ m/s, the agreement between the LES solution and the experiment and the empirical XFOIL model is particularly encouraging, while at $U_\infty = 37.7$ m/s some discrepancies appear downstream, consistent with increased sensitivity to the transitional behaviour of the boundary layer at lower Reynolds numbers, which is not fully resolved in the current Wall-Modelled LES. Transition onset and near-wall turbulence are known to be sensitive to the Reynolds number that affects the development of the boundary layer downstream of the trip, where small variations in the transition location of low-Re_c boundary layer flow can propagate downstream and produce measurable differences in wall shear stress [13–15]. Such Reynolds number dependent roughness sensitivity has also been reported for thick airfoil sections under low-Re_c conditions [28]. However, importantly, for both wind speeds, the WMLES solution for C_f agrees very well with the experiment around the trailing edge region at $x/c > 0.8$, which is more relevant for trailing edge noise.

3.1.2. *Meanflow velocity and turbulence profiles*

Figure 7 compares the wake profiles at a streamwise station just downstream of the trailing edge ($x/c = 1.0038$). The results are presented in terms of the normalised mean streamwise velocity, U_1/U_∞, and the wall-normal Reynolds stress, $\overline{u_2u_2}$. The profiles shown in Figs. 7a and 7b correspond to the high-speed case (U_∞ = 56 m/s), while those in Figs. 7c and 7d represent the lower-speed condition (U_∞ = 37.7 m/s).

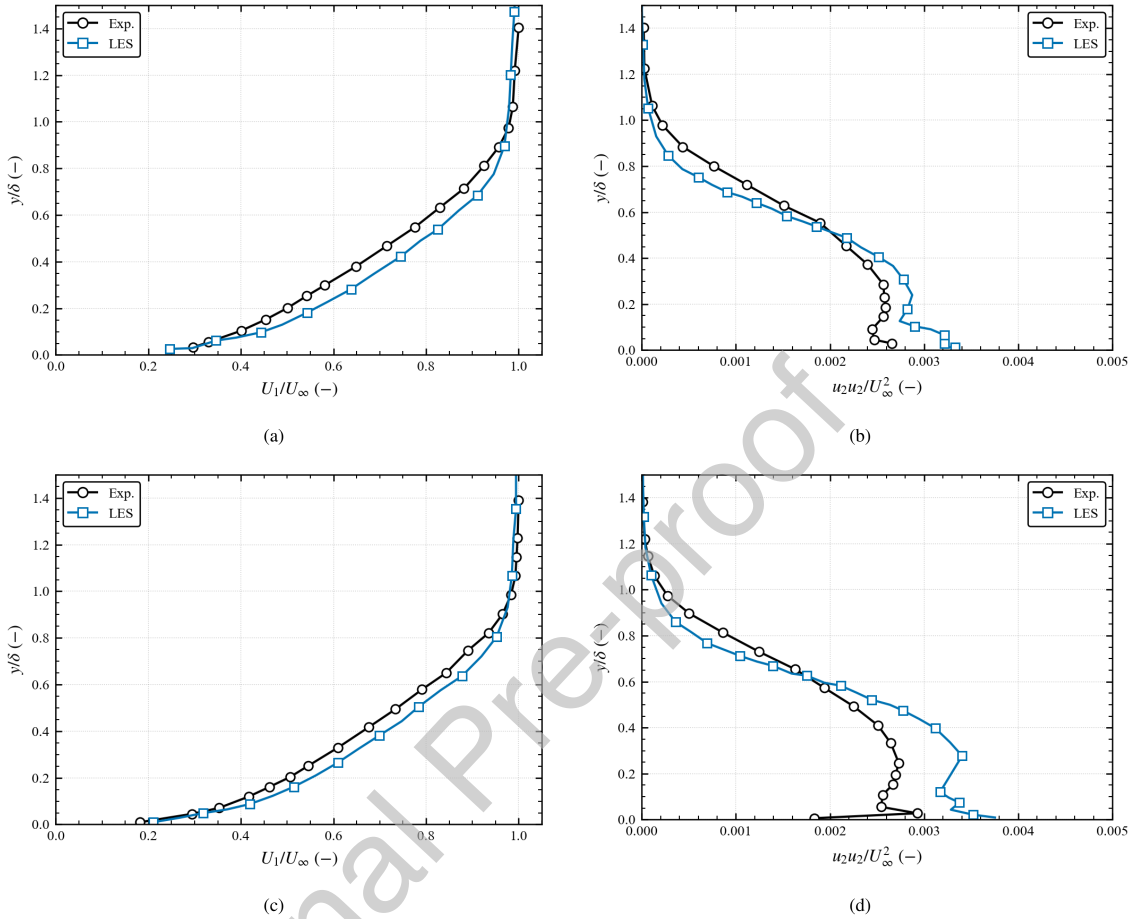

Figure 7: Comparison of boundary-layer profiles at x/c = 1.0038: mean velocity U_1/U_∞ for (a) $\mathrm{Re}_c = 1.5 \times 10^6$ and (c) $\mathrm{Re}_c = 1.0 \times 10^6$, and wall-normal Reynolds stress $\overline{u_2u_2}/U_\infty^2$ for (b) $\mathrm{Re}_c = 1.5 \times 10^6$ and (d) $\mathrm{Re}_c = 1.0 \times 10^6$. WMLES results (LES) are compared with the BANC-III experiment (Exp.).

For the mean velocity profiles Figs. 7a and 7c, the WMLES accurately reproduces the wake thickness and recovery rate at both wind speeds considered. At U_∞ = 56 m/s, the deviation between WMLES and experiment remains within $\Delta(U_1)/U_\infty \approx$ 0.02–0.05 across most of the measured boundary layer thickness, with slightly larger differences confined to the outer wake region. At U_∞ = 37.7 m/s, the deviation increases marginally in the outer region (up to $\approx$ 0.05), but the overall profile curvature and momentum deficit are well captured. This indicates that the boundary layer growth and wake development are predicted well in both Reynolds numbers. For wall-normal Reynolds stress distributions Figs. 7b and 7d, the WMLES captures the overall profile shape. The predicted decay of turbulent stresses with increasing y in the outer layer from the LES solution agrees well with the measurements. The LES also well predicts the location of the dominant near-wall peak, which occurs in the inner wake at approximately $y \approx 2.5$ mm for both flow conditions. However, the peak magnitude is over-predicted especially for the lower wind speed. At U_∞ = 56 m/s (Fig. 7b), the over-prediction of the WMLES solution of the peak stress value is approximately 11%.

At U_∞ = 37.7 m/s (Fig. 7d), the overestimation of the peak stress of the WMLES solution is about 20%. The larger error of the WMLES solution for the lower Reynolds number case is consistent with the previous discussion about the friction coefficient, which was found to be more difficult to predict accurately at a lower wind speed. The over-prediction of turbulent normal stress noted is consistent with trends reported in the WMLES literature, where resolved turbulence energy can exceed experimentally measured levels due to insufficient LES grid resolution as well as to the probe spatial filtering and signal processing in the experiment [4, 8, 19]. Similar discrepancies have also been documented in tripped boundary layer simulations when comparing high-fidelity numerical data with hot-wire measurements [42].

It can be noted that the fact that the present LES solution shows a larger discrepancy for the Reynolds stresses in comparison with the well-captured wall-shear-stress dependent friction coefficient at the trailing edge (Fig. 6) suggests that the internal structure of turbulence is still not fully recovered from the upstream tripping process. Such an "over-energized" state of the resolved fluctuations is a known numerical-physical artifact in WMLES, where the energy injected at the trip is not dissipated at the same rate as in the physical experiment due to the equilibrium wall model approximation and insufficient LES grid resolution.

3.1.3. Boundary layer integral properties

A summary of the boundary layer integral parameters computed from the LES solution is presented in Table 3. For $U_\infty = 56$ m/s, the WMLES predicts a boundary layer thickness within a relative error of approximately +2.0% in comparison with the experiment. The displacement thickness δ^* is over-predicted by about +2.7%, while the momentum thickness θ shows a larger deviation of approximately +8.4%. A similar trend is observed at $U_\infty =$ 37.7 m/s, where the boundary layer thickness is over-predicted by approximately +2.0% in comparison with the experiment, and the error in the predicted displacement thickness is less than 1%. Again, the error in momentum thickness is largest corresponding to approximately +6.9%. It can be noted that the consistently small discrepancies in δ and δ^* confirm that the integral wake thickness and mass deficit parameters are accurately reproduced, in agreement with the mean velocity profile solutions shown in Fig. 7.

Table 3: Turbulent boundary-layer integral parameters (suction side) derived from the mean velocity profile at $x_1/c = 1.0038$ for BANC-III Case 1 ($\mathrm{Re}_c = 1.5 \times 10^6$, $U_\infty = 56$ m/s, $\alpha = 0°$) and Case 4 ($\mathrm{Re}_c = 1.0 \times 10^6$,

$U_\infty = 37.7$ m/s, $\alpha = 0°$).

Case / Condition	Experiment			LES Simulation		
	δ (mm)	δ^* (mm)	θ (mm)	δ (mm)	δ^* (mm)	θ (mm)
Case 1: $\mathrm{Re}_c = 1.5 \times 10^6$, $U_\infty = 56$ m/s, $\alpha = 0°$	10.29	2.97	1.66	10.50	3.05	1.80
Case 4: $\mathrm{Re}_c = 1.0 \times 10^6$, $U_\infty = 37.7$ m/s, $\alpha = 0°$	10.74	3.14	1.75	10.96	3.12	1.87

It can be noted that the comparatively larger deviation in θ is not unexpected, since the momentum thickness depends on the detailed shape of the mean velocity profile through the momentum-deficit weighting and is therefore more sensitive to variations in the inner-to-mid layer than δ or δ^*. Consistent with this interpretation, Schlatter and Örlü [42] demonstrated using DNS that low-order integral quantities such as θ and the associated shape factor can exhibit measurable scatter depending on the inflow history and the tripping strategy, particularly at moderate Reynolds numbers. The present level of agreement, within approximately 10% for all integral measures, therefore, suggests that the mean flow development and overall wake growth are captured within similar fidelity as the turbulent boundary layer profiles discussed earlier.

3.1.4. Wall Surface Pressure Spectra

Figure 8 compares the wall surface pressure spectra close to the trailing edge for $U_\infty = 56$ m/s (Fig. 8a) and $U_\infty = 37.7$ m/s (Fig. 8b). In both cases, the spectra are purely broadband and representative of a fully turbulent boundary layer, with no evidence of transitional laminar-to-turbulent effects—such as tonal peaks—arising from the trip [2, 9, 10]. For $U_\infty = 56$ m/s, the LES solution shows excellent agreement with the experimental data in the frequency range $10^3 < f < 10^4$ Hz, with discrepancies generally remaining within the experimental uncertainty of ±1.5 dB reported in BANC-III [25]. While the difference becomes slightly larger at higher frequencies, it remains marginally within the allocated error bars. Similarly, the LES predictions for $U_\infty = 37.7$ m/s are in very good agreement with the measurements, staying largely within the ±1.5 dB threshold across all frequencies. These results suggest that the accuracy of the wall surface pressure spectra prediction is relatively insensitive to the Reynolds number variations considered here, especially when compared to the sensitivity typically observed in other turbulent boundary layer quantities.

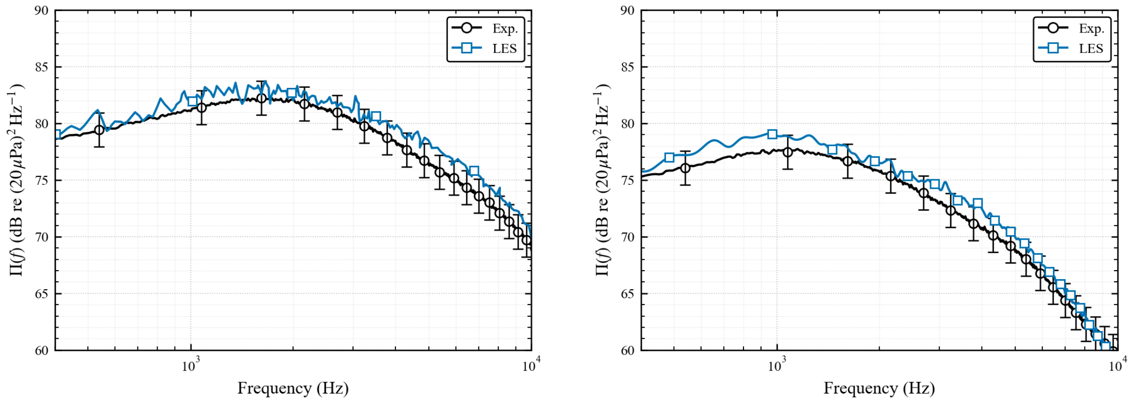

(a) (b)

Figure 8: Comparison of trailing-edge wall-pressure spectra at $x/c = 0.989$ and $\alpha = 0°$ for (a) $\mathrm{Re}_c = 1.5 \times 10^6$ and (b) $\mathrm{Re}_c = 1.0 \times 10^6$, comparing the WMLES predictions (LES) and BANC-III experiment (Exp.). Error bars of ±1.5 dB are included in accordance with the BANC-III uncertainty reported by Herr et al. [25].

3.1.5. Far-Field Noise Spectra

Figure 9 compares the predicted far-field sound pressure level at $\Theta = 90°$ to the free-stream flow at a distance of 1 m from the trailing edge (see Fig. 1) with the experimental measurements for $U_\infty = 56$ m/s and $U_\infty = 37.7$ m/s. Two sets of predictions based on the LES solutions are shown, one is using the Amiet model and the other is based on the BPM model. For $U_\infty = 56$ m/s, there is some discrepancy between solutions of the Aimet model and the BPM model. However, these discrepancies remain within the uncertainty of the BANC-III acoustic measurements that corresponds to ±2 dB. For $U_\infty = 37.7$ m/s, a similar level of agreement is observed up to the maximum frequency where the experimental data are available. Both the Amiet and the BPM solutions remain within the specified error bar of the acoustic measurements. However, a larger discrepancy between the Amiet model and the BPM noise spectra predictions can be seen at high frequencies ($f \gtrsim 6$ kHz), where the Amiet model prediction shows a much steeper spectrum roll-off compared to the BPM model.

It can be noted that this difference is likely due to the acoustic transfer function used in the Amiet model. Indeed, in the Amiet formulation, the farfield noise spectrum is obtained by convoluting the wall pressure spectrum through an acoustic transfer (scattering) function, whose magnitude decays rapidly at high frequencies, thereby producing a steeper high frequency roll-off even when the input wall surface pressure levels are comparable [6, 26]. In contrast, the BPM model applies a semi-empirical spectral shaping based on integral parameters of the boundary layer and functional dependencies obtained from curve-fitting [2]. However, since no reference experimental results are available for high frequencies here, it remains unclear which assumptions of the acoustic models considered are more appropriate in the case of low wind speed.

3.2. Sensitivity of Flow, Turbulence, and Noise Sources to Trip Parameters

3.2.1. Boundary layer profiles and wall surface pressure spectra

Figure 10 examines the influence of the trip geometry on the suction-side boundary layer for the wind speed case of $U_\infty = 37.7$ m/s. The effect of varying the trip height, width, and location on the mean flow velocity profiles, U_1/U_∞ just downstream of the trailing edge, $x/c = 1.0038$ are shown in Fig. 10(a,c,e) respectively. The effect of variation of the same trip parameters on the wall-normal Reynolds stress u_2u_2 is shown in Fig. 10(b,d,f) correspondingly. The same comparisons showing the sensitivity of the meanflow and turbulent velocity fluctuation profiles to the trip parameters for the higher velocity case $U_\infty = 56$ m/s are demonstrated in Fig. 11. As discussed earlier, the LES predictions for the higher wind speed case agree better with the experiment compared to the low speed case solutions. However, several common trends emerge, which are shared by the LES solutions regardless of the wind speed considered. First, the trip width and height have some influence on the wake profiles just downstream of the trailing edge. For variable trip widths, the mean velocity profiles for different widths collapse closely, however, there is some scatter

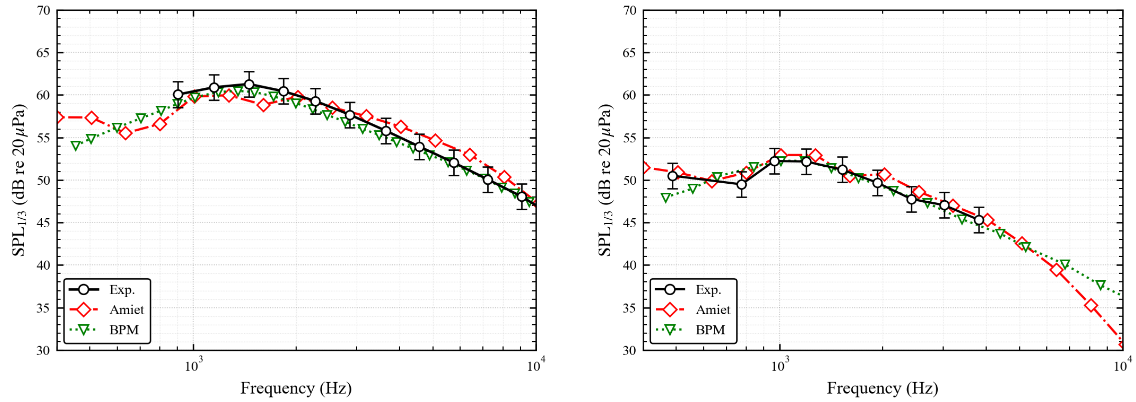

(a) (b)

Figure 9: Comparison of third-octave noise spectra for (a) $\mathrm{Re}_c = 1.5 \times 10^6$ and (b) $\mathrm{Re}_c = 1.0 \times 10^6$ predicted by the Amiet model and the BPM model based on the same LES solutions with the acoustic measurements (Exp.). The observer angle is $\Theta = 90°$, and the sound pressure level is normalised to a reference distance of 1 m.

in the u_2u_2 profiles suggesting some effect of the trip width on turbulent mixing. For the height variation, there is a stronger influence on both the meanflow velocity and Reynolds stress profiles. In particular, increasing h makes the wake thicker, indicating stronger momentum mixing and enhanced growth of the boundary layer. For the highest trip ($h = 1.018$ mm), larger deviations from the measurements are observed in the outer layer. In comparison with these, the mean-flow profiles corresponding to smaller heights are in better agreement with the mean-flow velocity profile from the experiment, although this leads to a thinner boundary layer. The effect of changing the trip height is also seen in a redistribution of turbulence intensity: while the smallest height case ($h = 0.127$ mm) shows the largest near-wall peak in u_2u_2, as h increases the magnitude of the inner-region peak reduces, spreading a larger part of the turbulent energy outward, in agreement with thickening of the boundary layer noted previously. The highest trip case ($h = 1.018$ mm) corresponds to a broader energetic region extending further into the outer layer, but with a lower maximum intensity near the wall. This suggests that larger roughness elements on the aerofoil surface promote earlier and more abrupt breakdown, leading to a thicker turbulent layer in which turbulent energy is mixed out over a larger wall normal region compared to the narrow zone near the wall that characterises small-scale roughness effects. In contrast to the above, a relatively low sensitivity of the boundary layer profiles at $x/c = 1.0038$ is found to the trip location. Although moving the trip changes the onset of the transition, the mean-flow velocity profile U_1/U_∞ remains fairly invariant to the trip location. The Reynolds stress profile u_2u_2 shows a small scatter mostly close to the wall. This suggests that the variations of the trip location considered are sufficiently small compared to the distance to the trailing edge not to affect the boundary layer state there. This behaviour is consistent with previous observations in the literature [42] that tripped boundary layers converge to similar downstream statistics despite some differences in the inflow history and tripping strategy. To further understand the origins of the sensitivity of the mean-flow velocity and turbulence in the developing boundary layer to the tip height, Fig. 12 compares the streamwise evolution of the mean profile and wall-normal Reynolds stress at $x/c = 0.30$, 0.70, and 1.00 for different trips. All trips are located at $x/c = 0.05$ and have the same width. At relatively small distances from the trip ($x/c = 0.30$), increasing the height of the trip h produces a marked increase in turbulence over a larger wall-normal distance, with the largest trip height leads to a substantial amplification of peak turbulence levels, u_2u_2 compared to the smaller trip heights. At larger downstream distances ($x/c = 0.70$), the peak turbulence levels corresponding to different trip heights reach more-or-less the same amplitude, while the boundary layer of the largest trip retains higher turbulence levels over a noticeably wider wall distance, indicating a pronounced effect of the initial perturbation due to the flow separation behind the trip. At the location of the trailing edge ($x/c = 1.00$), the growth of the peak turbulent intensity for the tallest trip is further slowed down compared to those of the narrower boundary layer profiles representative of the smaller trips. This can be related to a faster development of the hydrodynamic instability in thin boundary layers that have large velocity gradients compared to the broader boundary layer profile. At the same time, likely due to the turbulent diffusion mechanism, the difference between the boundary layer mean-flow and turbulence distributions corresponding to different trips at the trailing edge location important for noise is much smaller compared to the upstream locations. Fig. 13 compares the corresponding integral parameters of the boundary layer at the three different trip heights considered. Increasing h produces a systematically thicker boundary layer $\delta(x)$ across the chord, with the separation between the three trip cases becoming relatively less pronounced towards the trailing edge. The shape factor $H_{12}(x)$, defined as the ratio of displacement thickness to momentum thickness, is shown to decrease in the mid-chord region for the highest trip, consistent with the earlier transition and a broader boundary layer shape in this case. At the same time, near the trailing edge, the shape factors of all trip cases converge to the same value. Notably, the same trends of the effect of the trip height on the development of the boundary layer of the are also observed for the other case of wind speed U_∞ = 56 m/s, the results of which are not included here for brevity.

Section 3.2.1 compares the effect of the trip height and location on the wall pressure spectra close to the trailing edge location, x/c=0.989. Results for both wind speeds, U_∞ = 37.7 m/s and U_∞ = 56 m/s are shown in comparison with the experiment. First, it can be observed that there is a greater sensitivity to the trip height for the lower wind speed case U_∞ = 37.7 m/s compared to the higher speed case U_∞ = 56 m/s. In both cases, increasing the trip height to h = 1.018 mm leads to an improved agreement with the experiment compared to the original setup with h = 0.360 mm. However, because of the relatively large error bar (1.5dB) this improvement is marginally within the experimental uncertainty. Compared with some sensitivity to the height of the trip, the effect of variation of the trip location on the wall surface pressure spectra is completely negligible apart from mid-high frequencies around 2kHz which show some 1-2dB scatter for the low wind speed case.

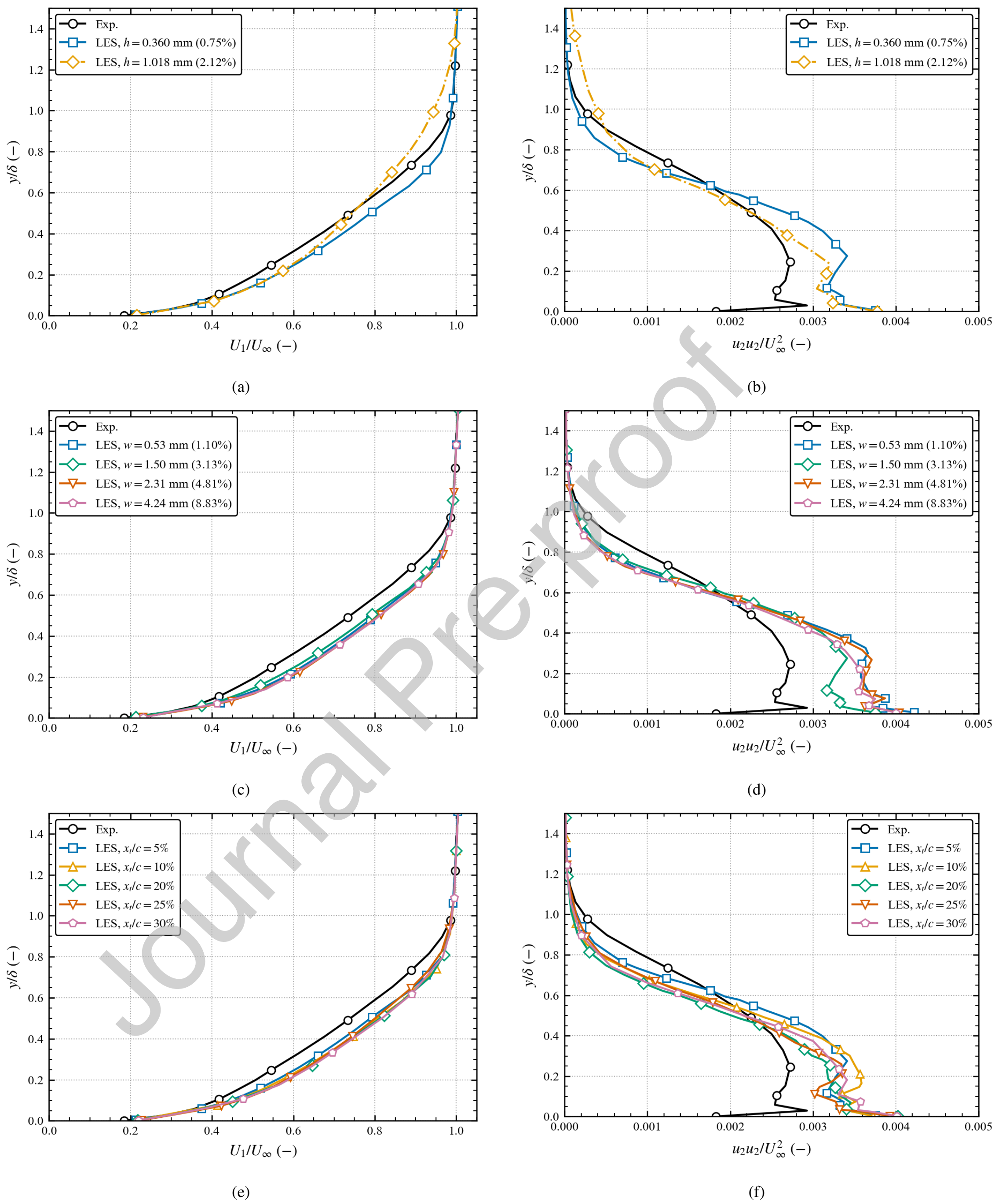

Figure 10: Effect of trip parameters on the boundary layer structure at x/c = 1.0038 and $\mathrm{Re}_c = 1.0 \times 10^6$: left column (a,c,e) shows the normalised mean velocity profiles U_1/U_∞ and right column (b,d,f) shows the corresponding wall-normal Reynolds stress distributions $\overline{u_2u_2}/U_\infty^2$. Rows correspond to variations in trip height (top), trip width (middle), and trip location (bottom). Experimental data (Exp. [25]) are included for reference.

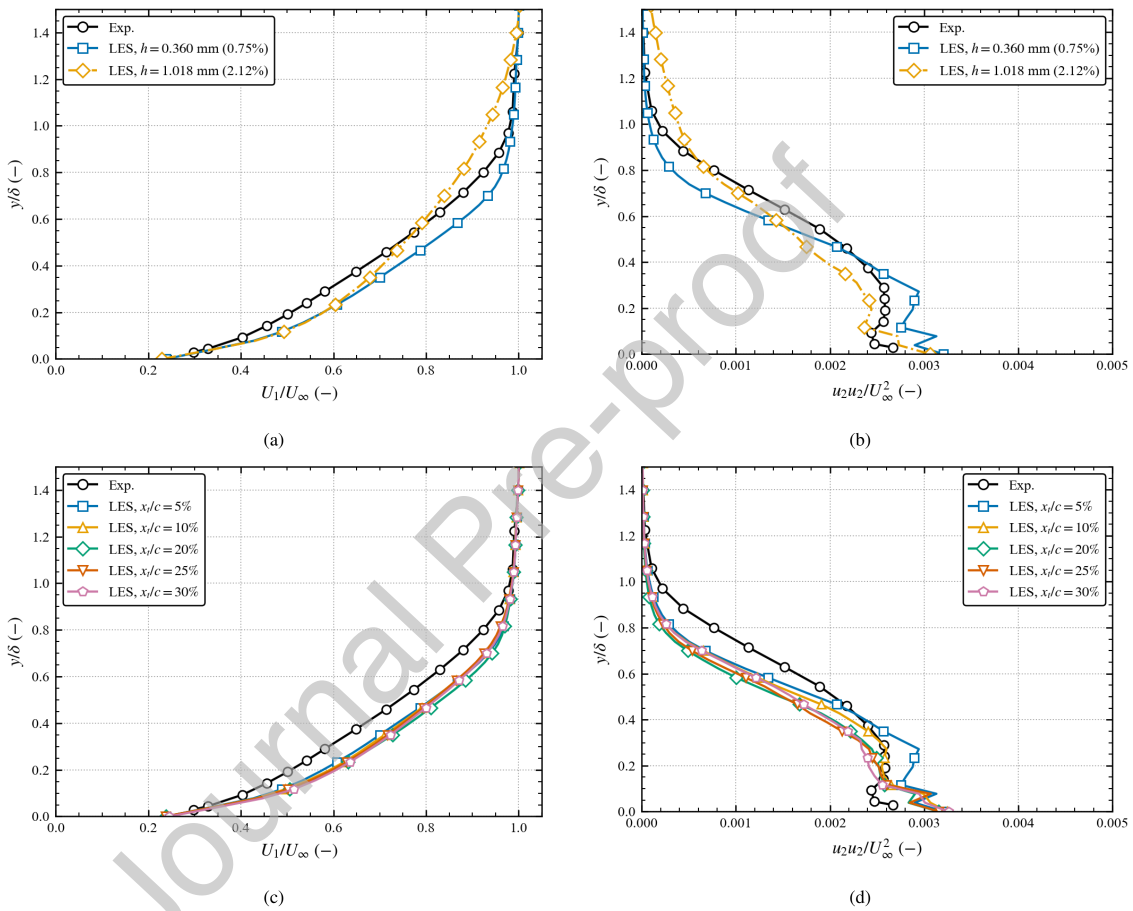

Figure 11: Effect of trip height and trip location on boundary layer structure at $x/c = 1.0038$ and $\mathrm{Re}_c = 1.5 \times 10^6$. The left column (a,c) shows the normalised mean velocity profiles U_1/U_∞ and the right column (b,d) shows the corresponding wall-normal Reynolds stress distributions $\overline{u_2u_2}/U_\infty^2$. The top row corresponds to variations in trip height, and the bottom row corresponds to variations in trip location. Experimental data (Exp. [25]) are included for reference.

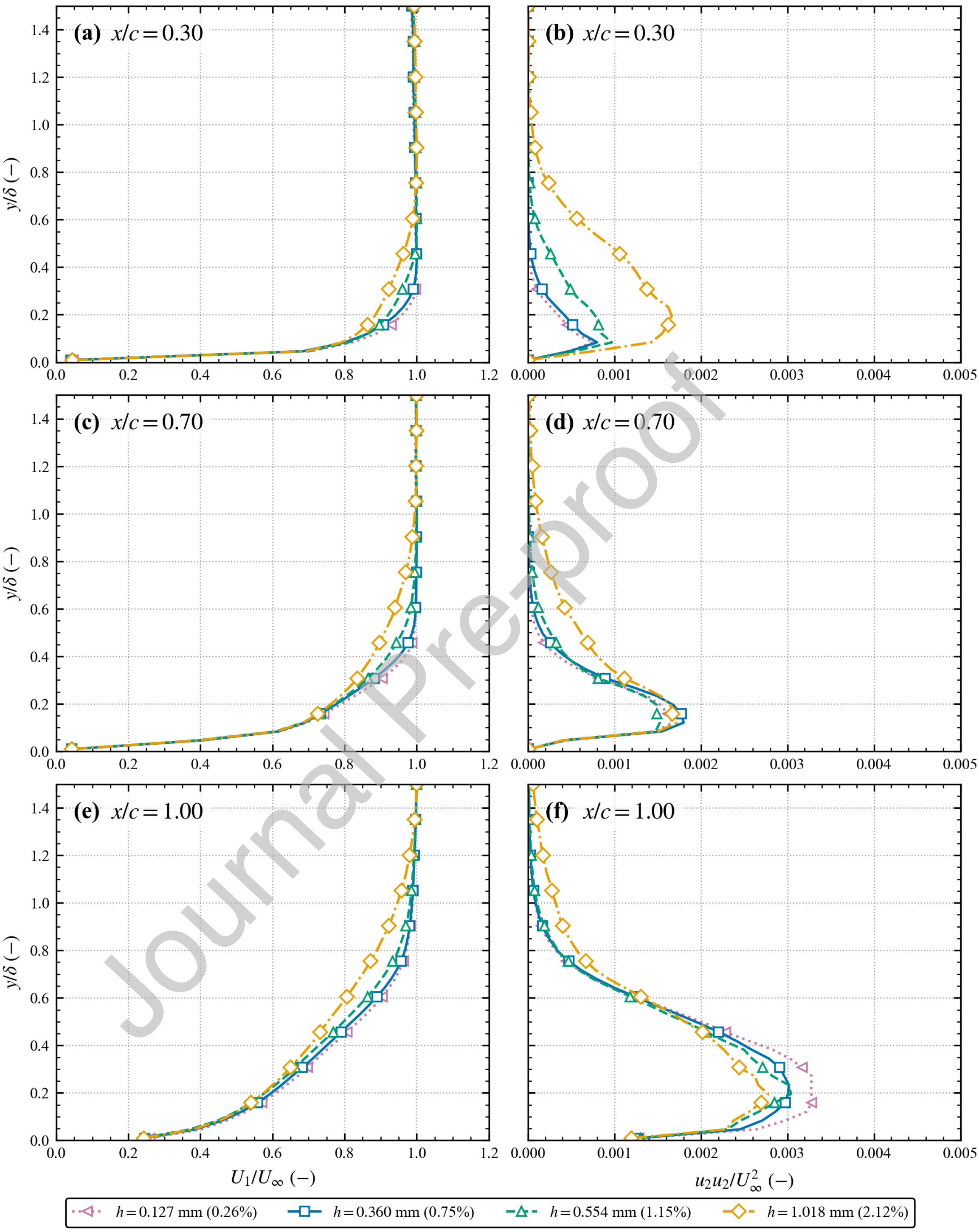

Figure 12: Evolution of boundary layer structure for varying trip height h at $\mathrm{Re}_c = 1.0 \times 10^6$. The left column (a,c,e) shows the normalised mean velocity profiles U_1/U_∞, while the right column (b,d,f) presents the corresponding wall-normal Reynolds stress distributions $\overline{u_2u_2}/U_\infty^2$. Profiles are shown at three streamwise stations: x/c = 0.30, 0.70, and 1.00. The results illustrate the influence of trip height on transition onset, turbulence development, and downstream recovery.

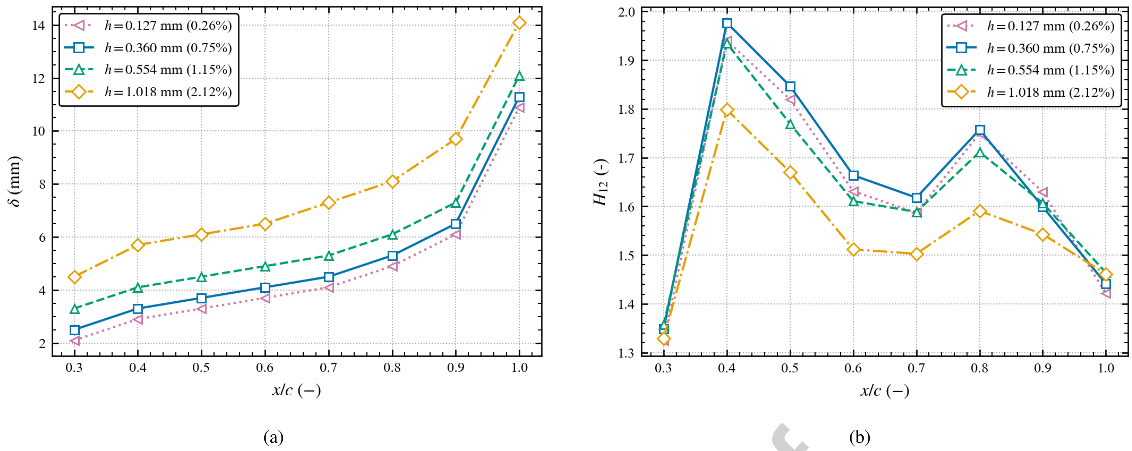

Figure 13: Influence of trip height h on integral boundary-layer parameters at $\mathrm{Re}_c = 1.0 \times 10^6$. The left panel shows the streamwise evolution of boundary layer thickness δ, while the right panel presents the corresponding shape factor $H_{12} = \delta^*/\theta$. Larger trip heights promote earlier transition and produce a thicker boundary layer downstream.

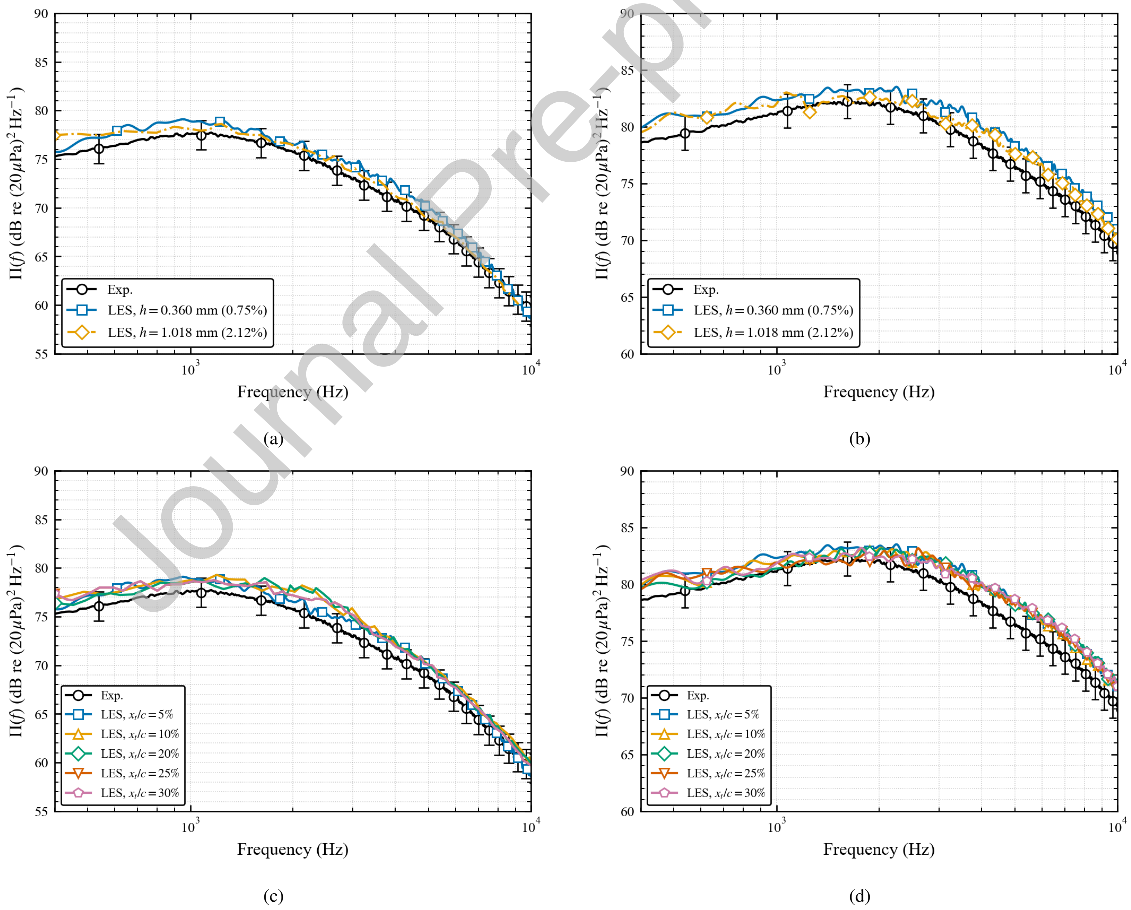

Figure 14: Effect of trip height (a,b) and trip location (c,d) on trailing-edge wall-pressure spectra. Left column (a,c): $\mathrm{Re}_c = 1.0 \times 10^6$; right column (b,d): $\mathrm{Re}_c = 1.5 \times 10^6$. Experimental measurements are shown for reference [25].

3.2.2. Proper Orthogonal Decomposition Analysis

A relatively weak dependence of the turbulence and wall pressure spectrum near the trailing edge on the trip parameters suggests that the dominant pressure structures in this region remain similar across different trip configurations. To test this hypothesis for the highest inflow velocity, the pressure fluctuations around the trailing edge are analyzed using Proper Orthogonal Decomposition (POD). A localized POD domain, covering 20% of the chord length in the streamwise direction and 4% in the vertical direction, is selected to focus specifically on the flow dynamics close to the trailing edge.

Figure 15 compares the modal energy distributions obtained using the first 50% and the full 100% of the available POD snapshots from the LES time signal for two extreme trip heights: the smallest (h = 0.127 mm) and the largest (h = 1.018 mm). Notably, the two modal energy distributions almost coincide for both cases. This confirms that the available LES time series are sufficiently long to ensure that the POD results are statistically converged and insensitive to the signal length. Furthermore, Fig. 16 compares the spatial distributions of several leading POD modes for these two trip heights.

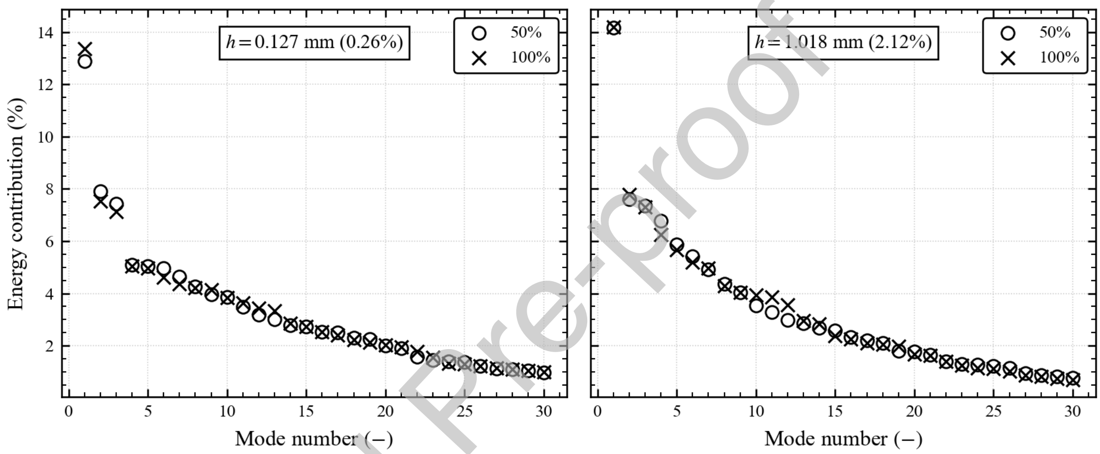

Figure 15: Relative modal energy for two trip heights: (a) h = 0.127 mm and (b) h = 1.018 mm. Results obtained using 50% and 100% of the available snapshots are compared, confirming negligible sensitivity of the energy distribution to the number of time samples.

Similarly to previous POD analyses for supercritical flows over cylinders at $Re_d \sim 0.4 \times 10^6$–$0.8 \times 10^6$ [43], the first POD mode ϕ_1 in the current cases exhibits an antisymmetric structure. To investigate whether this asymmetry stems from vortex shedding triggered by the trips on the top and bottom surfaces, a conditional averaging analysis is performed using the temporal coefficient of the first POD mode, $a_1(t)$, as a conditioning variable. The pressure fluctuation snapshots $Q(\boldsymbol{x}, t)$ are separated into two groups based on the sign of $a_1(t)$, specifically $a_1(t) > +\sigma_{a_1}$ and $a_1(t) < -\sigma_{a_1}$, where σ_{a_1} denotes the standard deviation of $a_1(t)$. These subsets are then used to compute the conditional difference fields:

$$\Delta Q(\boldsymbol{x}) = \langle Q \mid a_1 > +\sigma_{a_1} \rangle - \langle Q \mid a_1 < -\sigma_{a_1} \rangle. \quad (24)$$

Since the sign of $a_1(t)$ distinguishes between opposite phases of the dominant oscillation, this conditional difference effectively isolates the antisymmetric fluctuation pattern.

As shown in Fig. 16(b,g), the resulting field ΔQ closely resembles the first POD mode ϕ_1 in Fig. 16(a,f). This comparison confirms that the leading POD mode is directly related to the phase difference between the dominant coherent structures developing on the upper and lower airfoil surfaces. Consequently, the antisymmetry of the dominant POD mode is likely due to the fluctuating lift force originating from vortex shedding associated with the trips, consistent with previous experimental observations [43]. Higher-order POD modes (panels (c,h), (d,i) and (e,j)) are found to be largely symmetric and show similar distributions regardless of the trip height. This reinforces the conclusion that, despite upstream differences induced by the tripping devices, the dominant coherent flow structures in the trailing-edge region are weakly affected by the trip height and remain essentially unchanged.

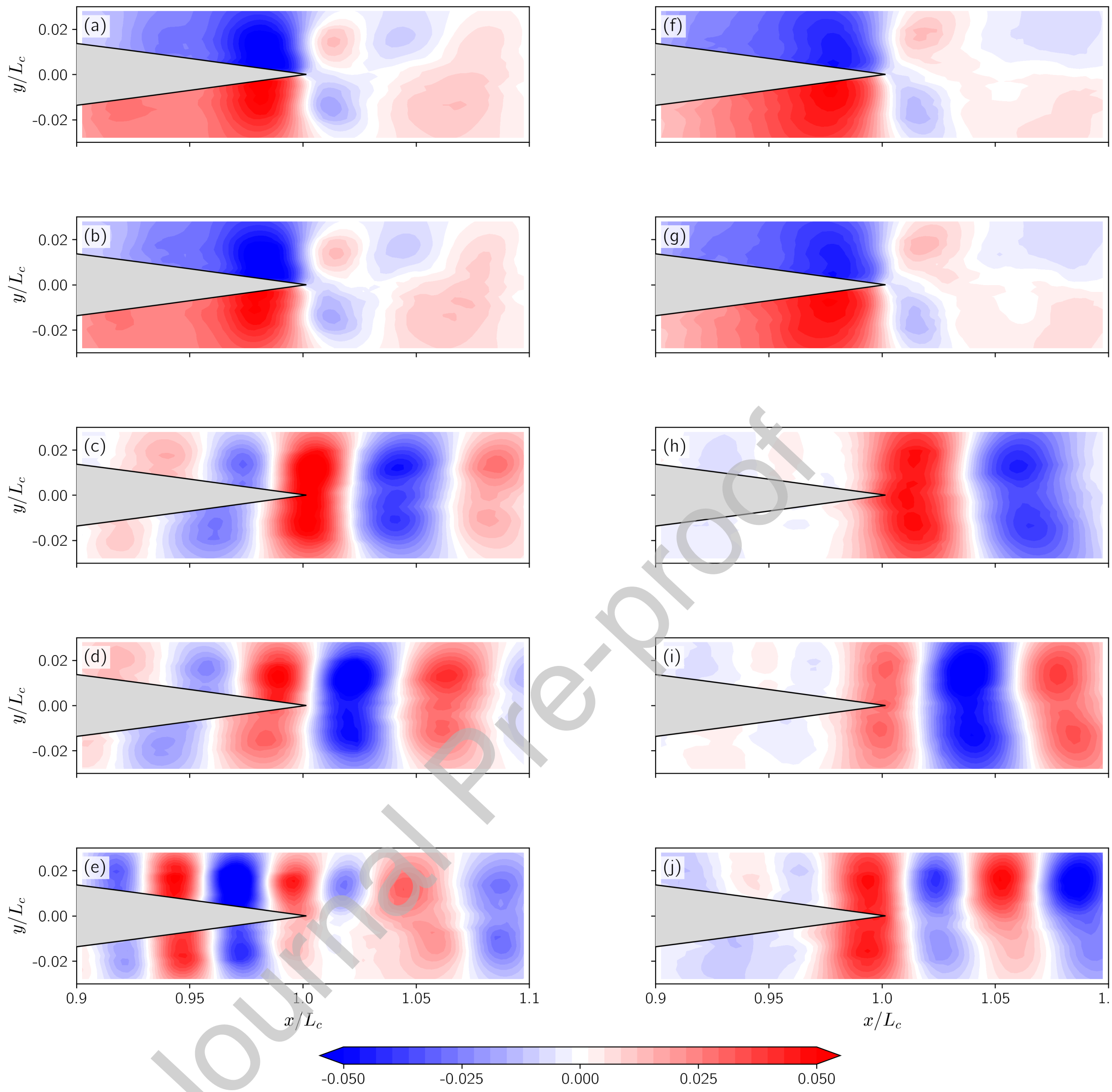

Figure 16: Spatial structures of the leading POD modes and of the conditionally-averaged difference field around the airfoil trailing edge, for two trip heights: left column (a–e) h = 0.127 mm and right column (f–j) h = 1.018 mm. All panels share the same dimensionless colour scale: the POD spatial modes $\phi_j(\mathbf{x})$ are unit-normalised eigenvectors ($\int \phi_j^2 \,\mathrm{d}\mathbf{x} = 1$), and the conditionally-averaged difference field ΔQ is scaled by $2\sigma_{a_1}$ so that $\Delta Q/(2\sigma_{a_1})$ is directly comparable in magnitude to ϕ_1. (a, f) First POD mode ϕ_1; (b, g) conditionally-averaged difference field ΔQ (Equation (24)); (c, h) second POD mode ϕ_2; (d, i) third POD mode ϕ_3; (e, j) fourth POD mode ϕ_4.

In conclusion, the consistency observed between the wall-pressure spectra, the POD modes, and the conditional averages demonstrates that the trailing-edge noise mechanisms are fundamentally governed by the fully developed turbulent boundary layer, exhibiting a remarkable robustness against variations in the upstream tripping conditions.

4. Conclusion

Wall-Modelled Large Eddy Simulations have been performed for the BANC III NACA 0012 airfoil configuration at zero angle of attack to investigate the effect of boundary-layer tripping on the mean flow, turbulence, wall-pressure fluctuations, and trailing-edge noise at two chord-based Reynolds numbers, $\mathrm{Re}_c = 1.0 \times 10^6$ and $\mathrm{Re}_c = 1.5 \times 10^6$. The numerical framework has first been validated against experimental measurements. Good agreement is obtained for the pressure and skin-friction coefficients, as well as for the mean velocity and Reynolds stress profiles near the trailing edge, particularly at the higher Reynolds number. The predicted wall-pressure spectra show limited sensitivity to grid resolution and agree with the experimental data within approximately ±1.5 dB. Far-field noise predictions obtained using the LES-informed Amiet theory and the BPM model also show good agreement with microphone measurements within the same uncertainty range. A parametric study of the trip geometry reveals that the trip height has the strongest influence on the boundary-layer development, especially at the lower Reynolds number. However, this influence progressively weakens towards the trailing edge, where the wall-pressure spectra become only weakly dependent on the trip configuration.

To explain this behaviour, Proper Orthogonal Decomposition of the pressure fluctuations in the trailing-edge region has been performed. The analysis shows that the dominant POD modes are well converged and largely insensitive to the trip height. The leading antisymmetric mode is associated with a phase difference between coherent structures developing on the upper and lower surfaces of the airfoil, as confirmed by conditional averaging of the pressure fluctuations. This behaviour is consistent with previous findings for bluff-body flows [43], and suggests that the dominant mode is linked to fluctuating lift induced by vortex-shedding mechanisms associated with the tripped boundary layers. The comparison between POD modes for different trip configurations indicates that the dominant coherent pressure structures near the trailing edge are only weakly affected by the trip height. This explains the observed robustness of the wall-pressure fluctuations, which represent the main source term for trailing-edge noise generation. As a result, within the range of trip parameters considered here, the far-field acoustic response is found to be only weakly sensitive to the details of the trip geometry.

Declaration of interests

The authors declare that they have no known competing financial interests or personal relationships that could have appeared to influence the work reported in this paper.

Acknowledgement

The authors would like to acknowledge the Engineering and Physical Sciences Research Council (EPSRC) for supporting this research (Grant No. EP/V038222/1). The authors also acknowledge the use of Tier-2 high-performance computing (HPC) facility JADE-2, funded by the EPSRC on the grant (EP/T022205/1) and Queen Mary's Apocrita HPC facility, supported by QMUL Research-IT. http://doi.org/10.5281/zenodo.438045.

References

[1] T. F. Brooks, T. H. Hodgson, Trailing edge noise prediction from measured surface pressures, J. Sound Vib. 78 (1) (1981) 69–117. doi:10.1016/S0022-460X(81)80158-7.

[2] T. F. Brooks, D. S. Pope, M. A. Marcolini, Airfoil self-noise and prediction, Tech. Rep. NASA RP-1218, NASA, Hampton, Virginia (1989).

[3] S. A. Rizzi, D. L. Huff, D. D. J. Boyd, P. Bent, B. S. Henderson, K. A. Pascioni, D. C. Sargent, D. L. Josephson, M. Marsan, H. He, R. Snider, Urban air mobility noise: Current practice, gaps, and recommendations, Tech. Rep. NASA/TP–2020-5007433, National Aeronautics and Space Administration (NASA), Hampton, Virginia (2020). doi:10.2514/6.2020-5007433.

[4] J. Winkler, S. Moreau, T. Carolus, Airfoil trailing edge noise prediction from large-eddy simulation: Influence of grid resolution and noise model formulation, in: 16th AIAA/CEAS Aeroacoustics Conference, American Institute of Aeronautics and Astronautics, Stockholm, Sweden, 2010. doi:10.2514/6.2010-3704.

[5] W. R. Wolf, S. K. Lele, Trailing-edge noise predictions using compressible large-eddy simulation and acoustic analogy, AIAA J. 50 (11) (2012) 2423–2434. doi:10.2514/1.J051638.

[6] R. K. Amiet, Noise due to turbulent flow past a trailing edge, J. Sound Vib. 47 (3) (1976) 387–393. doi:10.1016/0022-460X(76)90948-2.

[7] X. Gloerfelt, The link between wall pressure spectra and radiated sound from turbulent boundary layers, in: 16th AIAA/CEAS Aeroacoustics Conference, American Institute of Aeronautics and Astronautics, Stockholm, Sweden, 2010. doi:10.2514/6.2010-2904.

[8] M. Mehrabadi, D. J. Bodony, Wall-modeled large-eddy simulation and direct numerical simulation of broadband trailing edge noise from a NACA 0012 airfoil, in: 25th AIAA/CEAS Aeroacoustics Conference, American Institute of Aeronautics and Astronautics, Delft, The Netherlands, 2019. doi:10.2514/6.2019-2643.
[9] A. Samson, S. Sarkar, Effects of free-stream turbulence on transition of a separated boundary layer over the leading-edge of a constant thickness airfoil, J. Fluids Eng. 138 (2) (2015) 021202. doi:10.1115/1.4031249.
[10] S. Pröbsting, S. Yarusevych, Laminar separation bubble development on an airfoil emitting tonal noise, J. Fluid Mech. 780 (2015) 167–191. doi:10.1017/jfm.2015.427.
[11] T. J. Mueller, Aeroacoustic Measurements, Springer-Verlag, Berlin, Germany, 1990.
[12] N. Tabatabaei, R. Vinuesa, R. Örlü, P. Schlatter, Techniques for turbulence tripping of boundary layers in RANS simulations, Flow Turbul. Combust. 108 (2022) 661–682. doi:10.1007/s10494-021-00296-5.
[13] H. A. Abdalla, Boundary layer-tripping studies on characteristics of near-wake behind a cambered airfoil, Eng. Res. J. 22 (3) (1999) 115–133. doi:10.21608/erjm.1999.72455.
[14] M. S. Chandrasekhara, M. C. Wilder, L. W. Carr, Boundary-layer-tripping studies of compressible dynamic stall flow, AIAA J. 34 (1) (1996) 96–101. doi:10.2514/3.13027.
[15] F. L. dos Santos, C. H. Venner, L. de Santana, Tripping device effects on the turbulent boundary layer development, in: AIAA AVIATION 2022 Forum, American Institute of Aeronautics and Astronautics, Chicago, Illinois, 2022. doi:10.2514/6.2022-3332.
[16] M. V. Morkovin, On roughness — induced transition: Facts, views, and speculations, in: M. Y. Hussaini, R. G. Voigt (Eds.), Instability and Transition, ICASE/NASA LaRC Series, Springer, New York, NY, 1990, pp. 281–295. doi:10.1007/978-1-4612-3430-2_34.
[17] H. Schlichting, K. Gersten, Boundary-Layer Theory, 9th Edition, Springer-Verlag, Berlin, Germany, 2016.
[18] D. Kang, S. Lee, Aerodynamic and aeroacoustic effects of different transition mechanisms on an airfoil, AIAA J. 62 (4) (2024) 1517–1535. doi:10.2514/1.J063270.
[19] J. Winkler, H. Wu, S. Moreau, T. Carolus, R. D. Sandberg, Trailing-edge broadband noise prediction of an airfoil with boundary-layer tripping, J. Sound Vib. 482 (2020) 115450. doi:10.1016/j.jsv.2020.115450.
[20] N. Morse, K. Mahesh, Tripping effects on model-scale studies of flow over the DARPA SUBOFF, J. Fluid Mech. 975 (2023) A3. doi:10.1017/jfm.2023.777.
[21] S. Luesutthiviboon, L. T. Lima Pereira, D. Ragni, F. Avallone, M. Snellen, Aeroacoustic benchmarking of trailing-edge noise from NACA 63 3-018 airfoil with trailing-edge serrations, AIAA J. 61 (1) (2023) 329–354. doi:10.2514/1.J061630.
[22] S. Karabasov, V. Goloviznin, Compact accurately boundary-adjusting high-resolution technique for fluid dynamics, J. Comput. Phys. 228 (2009) 7426–7451. doi:10.1016/j.jcp.2009.06.037.
[23] V. A. Semiletov, S. A. Karabasov, CABARET scheme with conservation-flux asynchronous time-stepping for nonlinear aeroacoustics problems, J. Comput. Phys. 253 (2013) 157–165. doi:10.1016/j.jcp.2013.07.008.
[24] A. P. Markesteijn, S. A. Karabasov, Large eddy simulation and acoustic modelling of an installed jet configuration of industrial complexity on graphics processing units, Appl. Acoust. 224 (2024) 110159. doi:10.1016/j.apacoust.2024.110159.
[25] M. Herr, R. Ewert, C. Rautmann, M. Kamruzzaman, D. Bekiropoulos, A. Iob, R. Arina, P. Batten, S. Chakravarthy, F. Bertagnolio, Broadband trailing-edge noise predictions — overview of BANC-III results, in: 21st AIAA/CEAS Aeroacoustics Conference, American Institute of Aeronautics and Astronautics, Dallas, Texas, 2015. doi:10.2514/6.2015-2847.
[26] M. Roger, S. Moreau, Back-scattering correction and further extensions of Amiet's trailing-edge noise model. Part 1: theory, J. Sound Vib. 286 (3) (2005) 477–506. doi:10.1016/j.jsv.2004.10.054.
[27] A. L. Braslow, E. C. Knox, Simplified method for determination of critical height of distributed roughness particles for boundary-layer transition at Mach numbers from 0 to 5, Tech. Rep. NACA TN 4363, National Advisory Committee for Aeronautics (NACA), Washington, DC (1958).
[28] R. P. J. O. M. van Rooij, W. A. Timmer, Roughness sensitivity considerations for thick rotor blade airfoils, J. Sol. Energy Eng. 125 (4) (2003) 468–478. doi:10.1115/1.1624614.
[29] P. Balakumar, P. S. Iyer, Laminar to turbulence transition in boundary layers due to tripping devices, in: AIAA SciTech Forum, AIAA Fluid Dynamics Conference, American Institute of Aeronautics and Astronautics, Virtual Event, 2021. doi:10.2514/6.2021-1948.
[30] A. Chintagunta, S. E. Naghibi, S. A. Karabasov, Flux-corrected dispersion-improved CABARET schemes for linear and nonlinear wave propagation problems, Comput. Fluids 169 (2018) 111–128. doi:10.1016/j.compfluid.2017.08.018.
[31] A. P. Markesteijn, S. A. Karabasov, CABARET solutions on graphics processing units for NASA jets: Grid sensitivity and unsteady inflow condition effect, C. R. Méc. 346 (10) (2018) 948–963. doi:10.1016/j.crme.2018.07.004.
[32] V. M. Goloviznin, V. N. Semenov, I. A. Korotkin, S. A. Karabasov, A novel computational method for modelling stochastic advection in heterogeneous media, Transp. Porous Media 66 (3) (2007) 439–456. doi:10.1007/s11242-006-0005-7.
[33] V. A. Semiletov, S. A. Karabasov, A volume integral implementation of the Goldstein generalised acoustic analogy for unsteady flow simulations, J. Fluid Mech. 853 (2018) 461–487. doi:10.1017/jfm.2018.411.
[34] V. A. Semiletov, S. A. Karabasov, CABARET scheme for computational aero acoustics: Extension to asynchronous time stepping and 3D flow modelling, Int. J. Aeroacoust. 13 (3-4) (2014) 321–336. doi:10.1260/1475-472X.13.3-4.321.
[35] G. I. Park, Wall-modeled large-eddy simulation of a separated flow over the NASA wall-mounted hump, Annu. Res. Briefs CTR (2015) 145–160.
[36] T. Mukha, S. Rezaeiravesh, M. Liefvendahl, A library for wall-modelled large-eddy simulation based on OpenFOAM technology, Comput. Phys. Commun. 239 (2019) 204–224. doi:10.1016/j.cpc.2019.01.016.
[37] H. A. Abid, A. P. Markesteijn, S. A. Karabasov, Trailing edge noise modelling of flow over NACA airfoils informed by LES, in: AIAA AVIATION 2021 Forum, American Institute of Aeronautics and Astronautics, Virtual Event, 2021. doi:10.2514/6.2021-2233.
[38] H. A. Abid, A. P. Markesteijn, S. A. Karabasov, B. Zang, M. Azarpeyvand, Y. D. Mayer, Improving accuracy of airfoil trailing edge noise models with turbulent flow anisotropy, in: 28th AIAA/CEAS Aeroacoustics Conference, American Institute of Aeronautics and Astronautics, Southampton, United Kingdom, 2022. doi:10.2514/6.2022-3105.
[39] O. Stalnov, P. Chaitanya, P. F. Joseph, Towards a non-empirical trailing edge noise prediction model, J. Sound Vib. 372 (2016) 50–68.

doi:10.1016/j.jsv.2015.10.011.
[40] J. L. Lumley, The structure of inhomogeneous turbulent flows, in: A. M. Yaglom, V. I. Tatarski (Eds.), Atmospheric Turbulence and Radio Wave Propagation, Nauka, Moscow, USSR, 1967, pp. 166–178.
[41] L. Sirovich, Turbulence and the dynamics of coherent structures. Parts I–III, Q. Appl. Math. 45 (3) (1987) 561–590. doi:10.1090/qam/910462.
[42] P. Schlatter, R. Örlü, Turbulent boundary layers at moderate Reynolds numbers: inflow length and tripping effects, J. Fluid Mech. 710 (2012) 5–34. doi:10.1017/jfm.2012.316.
[43] Y. Qiu, Y. Sun, Y. Wu, Y. Tamura, Analyzing the fluctuating pressures acting on a circular cylinder using stochastic decomposition, J. Fluids Struct. 50 (2014) 512–527. doi:10.1016/j.jfluidstructs.2014.07.008.